

6G for Connected Sky

“6G-SKY”

Work Package 2

Multi-Technology Connectivity Links

Task 2.2 – ATG Antenna Development Specific for Flying Vehicles

Deliverable 2.2.1

Simulation Framework for Investigation of Antennas Integrated in Flying Vehicles and Their Performance in Real-World 3D Network Scenarios.

6G-SKY Project
01. Feb. 2023



Abstract

The 6G-SKY project aims at holistic solutions to enable reliable and robust connectivity for aerial and ground users. The main goal of WP2 is to define and proof the best link parameter and antenna systems for the different challenges of the NTN communication channels. Task 2.2.1 aims at developing a simulation framework that allows the design of new antenna concepts to serve aerial user equipment and evaluate their performance in a real-world 3D network scenario. This document introduces a simulation framework focusing on direct air-to-ground communications, although other use cases relevant for the 6G-SKY project are readily supported as well. The simulation framework consists of two main components: antenna design and system-level formulation. The antenna design is guided by a link budget and array dimensioning based on the system requirements and deployment assumptions which provide the specifications for the radiator, array, and beamforming design. Full electromagnetic simulations are performed, and embedded antenna element patterns and other antenna performance indicators are provided to system-level simulations. Considering 3D deployment scenarios, the system-level simulators provide network-level key performance indicators, and it can be determined whether the antenna design satisfies the system requirements.

Participants in WP 2:

- Deutsche Telekom (WPL, TL)
- EAB (TL)
- KTH
- Fraunhofer
- Airbus
- EAG (TL)

Contributors in Task 2.2

- EAG (TL)
- Airbus
- Deutsche Telekom

6G-SKY, Work Package 2: Multi-Technology Connectivity Links

Task 2.2: ATG antenna development specific for flying vehicles

Sub-Task 2.2.1: A simulation framework will be established that enables the investigation of antennas integrated in flying vehicles and their performance in real world 3D network scenarios.

D2.2.1 Simulation framework

Editor: Lucas Nogueira Ribeiro, Ericsson Antenna Technology Germany GmbH (EAG)

Reviewer: Jan Graevendieck, (EAG)

Contributors: Sertan Hastürkoglu, Martin Jacob, Jan Graevendieck, Philipp Gentner, Tobias Mann (EAG)

6G-SKY

Deliverable 2.2.1

Editor: Lucas Nogueira Ribeiro, EAG

Project coordinator: Dominic Schupke, Airbus

Technical Project Coordinator

CELTIC published project result

© 2023 CELTIC-NEXT

Disclaimer for confidential CELTIC-Plus project reports

This document contains material, which is copyright of certain PARTICIPANTS and may not be reproduced or copied without permission. The information contained in this document is the proprietary confidential information of certain PARTICIPANTS and may not be disclosed except in accordance with the regulations agreed in the Project Consortium Agreement (PCA).

The commercial use of any information in this document may require a licence from the proprietor of that information.

Neither the PARTICIPANTS nor CELTIC-NEXT warrant that the information contained in this document is capable of use, or that use of the information is free from risk and accept no liability for loss or damage suffered by any person using the information.



Document History

Version	Date	Author(s)/Reviewer	Comment
1.0	03.02.2023	EAG	Internal draft
1.1	17.02.2023	EAG	First submission
1.2	06.11.2025	Jan Graevendieck	Confidential removed

Executive Summary

This document presents a simulation framework for development and performance evaluation of antenna systems tailored for direct air-to-ground communications. The simulation framework lays the fundamentals of the antenna systems to be designed in WP2 and experimentally demonstrated in WP5. A state-of-the-Art review is presented in this document to help identifying the limitations and existing challenges in current direct air-to-ground antenna solutions. Promising research directions related to radiator design, array technology, and beamforming strategies are indicated and shall guide the work in the future work package tasks. Ericsson Antenna Systems benefits from the novel active antenna system concepts, including radiator and array designs for the over-6-GHz spectrum, and state-of-the-Art dynamic and energy-efficient beamforming strategies. Furthermore, Ericsson Antenna Systems also benefits from the antenna evaluation methodology introduced in this document, which can be readily adapted to other 6G enabling technologies. In conclusion, the simulation framework introduced in this deliverable enables the novel design, evaluation, and experimental work to be done in the upcoming tasks.



List of Authors

- Lucas Nogueira Ribeiro (Ericsson Antenna Systems, Germany)
- Sertan Hastürkoglu (Ericsson Antenna Systems, Germany)
- Martin Jacob (Ericsson Antenna Systems, Germany)
- Philipp Karl Gentner (Ericsson Antenna Systems, Germany)
- Jan Graevendieck (Ericsson Antenna Systems, Germany)
- Tobias Mann (Ericsson Antenna Systems, Germany)

Table of Contents

Abstract	2
Document History	4
Executive Summary	5
List of Authors	6
Table of Contents	7
List of Abbreviations	8
1 Introduction	9
1.1 Objective.....	9
1.2 Structure of the Document.....	10
2 State-of-the-Art Review	11
3 System Model.....	13
3.1 Network Requirements	13
3.2 Antenna Requirements.....	13
3.2.1 Ground Station Antenna Requirements.....	14
3.2.2 Aircraft Antenna Requirements	15
3.3 Network and Radio Access Technology Models.....	15
3.4 Propagation Model.....	17
3.5 Antenna Array Model	17
3.5.1 Equal Embedded Element Pattern Case	21
3.5.2 AoSA Beampattern Examples.....	21
4 Simulation Framework	22
4.1 Link Budget Analysis	23
4.2 AAS Dimensioning.....	24
4.3 Antenna Design	31
4.3.1 Ground Station Antenna.....	33
4.3.2 Aircraft Antenna.....	34
4.4 Beamforming Design.....	36
4.5 Network-Level Simulator	37
5 Conclusion.....	38
6 References	39

List of Abbreviations

AAS	Active antenna system
AF	Array factor
AoSA	Array of sub-arrays
ATG	Air to ground
BS	Base station
CPD	Cross-polar discrimination
CPE	Customer premise equipment
CSI	Channel state information
DFT	Discrete Fourier transform
DL	Downlink
EIRP	Effective isotropic radiated power
FDD	Frequency division duplexing
GoB	Grid of beams
GS	Ground station
HAPS	High-altitude platforms
HIBS	HAPS as IMT base stations
HPBW	Half-power beamwidth
ISD	Inter-site distance
KPI	Key performance indicator
LOS	Line of sight
MIMO	Multiple-input multiple-output
MISO	Multiple-input single-output
NLOS	Non-line of sight
NR	New radio
NTN	Non-terrestrial networks
RAT	Radio access technology
RB	Resource block
RET	Remote electrical tilt
RSRP	Reference signal received power
SINR	Signal to interference and noise ratio
SL	Sidelobe
SLL	Sidelobe level
TDD	Time division duplexing
TN	Terrestrial networks
TRP	Total radiated power
UAV	Unmanned aerial vehicle
UE	User equipment
UL	Uplink
ULA	Uniform linear array
URA	Uniform rectangular array
WP	Work package

1 Introduction

The 6G-SKY project aims at solutions to enable reliable and robust connectivity for aerial and ground users via flexible and adaptive network architecture adopting multiple technologies such as satellite and direct air-to-ground (ATG) communications.

The main goal of WP2 is to define and proof the best link parameters and antenna systems for the different challenges of the NTN communication channels. This provides input to for network design for flying users and for design of NTN for terrestrial users. This document is the first deliverable of Task 2.2, and it introduces a simulation framework that enables the performance evaluation of the novel antenna concepts to be developed in this project. The 6G SKY project investigates different NTN use cases, each with specific requirements. Therefore, the proposed antenna simulation framework shall be flexible to consider the use cases of interest [1]. The first use case to be investigated is ATG communications. Later, the simulation framework shall be employed to design and evaluate antennas for unmanned aerial vehicles (UAVs) and flying taxis.

The general architecture of the simulation framework is illustrated in the flowchart of Figure 1.1.1. It consists mainly of two steps: antenna design and system-level performance evaluation. The former step takes requirements and design parameters as inputs. A sophisticated antenna design methodology is used to design and simulate the antenna system and generate the necessary data for system-level evaluation of the antenna. In particular, the antenna beampatterns and their corresponding beamforming weights are central for the network-level assessment of the antenna system. If the antenna design does not satisfy the requirement criteria, then it should be redesigned by either recalculating the antenna parameter or relaxing the requirements.

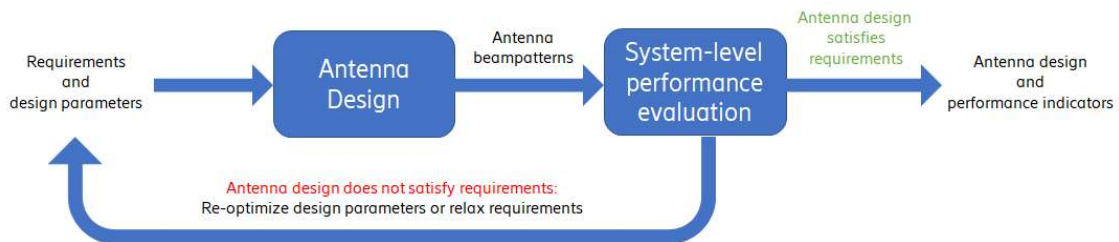


Figure 1.1.1 Simulation framework flowchart.

1.1 Objective

The primary objective of this document is to present a simulation framework for NTN antenna systems using ATG as the first use case of interest. The simulation framework shall support the evaluation of both electromagnetic and network aspects of advanced antenna systems. Furthermore, the framework shall enable the assessment some of the KPIs discussed in WP1. These simulation framework requirements shall enable the development of new antenna concepts that outperform the existing ATG solutions.

Simulation frameworks are based on system models. Therefore, the secondary objectives aim at characterizing the system model for the simulation framework.



They read as follows:

- To survey the state-of-the-art review of ATG antenna solutions to identify the main challenges and limitations of the current technology.
- To identify and discuss the relevant antenna and system requirements and present some design assumptions.
- To elaborate an ATG design and simulation framework, including antenna dimensioning, full electromagnetic simulation of the antenna array, and optimization of beamforming weights.

1.2 Structure of the Document

This document is structured as follows: Chapter 2 provides a state-of-the-Art review on ATG antenna technologies. In Chapter 3, the system model in which the simulation framework is based upon is presented. This chapter discusses system requirement assumptions, and the network, propagation, and antenna models. Chapter 4 presents the simulation framework in detail. The chapter is divided into link budget analysis, antenna dimensioning, radiator and array design, beamforming design, and network-level simulation. The concluding remarks are presented in Chapter 5 and the references are listed in Chapter 6.



2 State-of-the-Art Review

State of the art broadband access of airplanes at cruising altitude is usually provided via SatCom and/or wireless terrestrial based ATG links. This section aims to summarize existing solutions and ongoing global activities for the latter technology. The focus lies on the antennas located at both, the ground station (GS) as well as the flying vehicles.

The most prominent existing large scale broadband ATG networks are the European Aviation Network (EAN) (Europe), SmartSky (US) and GoGo (US).

	EAN	GoGo 5G	Smart Sky
Frequency	LTE B65 (2x 15 MHz) 2170-2185 MHz DL 1980-1995 MHz UL	2423 MHz - 2475 MHz	ISM (2x30 MHz) 2407.8-2437.8 MHz DL 2445.7-2475.7 MHz UL
Technology	LTE (with proprietary adaptations)	CDMA/5G O-RAN	LTE
BS antenna	2T2R MIMO sector antennas, 2x40W (46 dBm)	16T/16R antennas	8T/8R antennas
UE	Fuselage antennas, 37 dBm transmit power	Fuselage mounted “blade style multiband phased array”	2x diversity fuselage mounted blade antennas, 34dBm TX power per port

Table 2.1 State of the art ATG networks and their operating frequencies.

The terrestrial part of the European Aviation network is operated by Deutsche Telekom. Roll-out has been done by Nokia (now SkyFive) until 2018. The network employs ~300 proprietary base stations Europe based on LTE technology. The antennas are often installed at high elevation sites and uses LTE band 65 in a three-sector configuration. Their radiation characteristics are optimized for serving airplanes at altitudes between 3000 and 10000 meters. Maximum transmit power is 2x40 W (46 dBm). The UE/airplane hardware exhibits AceAxis radio heads (37 dBm transmit power) connected to antennas at the lower fuselage [2].

The US based GoGo network started with a nationwide network based on CDMA technology. Recently GoGo updated its 150 sites across the USA to 5G with 16 port beamforming antennas together with AIRSPAN 5G NR radio heads. Similar to EAN a modem together with two “blade style multiband phased array” antennas at the fuselage is used at the airplane side [3] [4].

The SmartSky network operates at the 2.4 GHz ISM band and exhibits sites up to 12 sectors covering up to 180 miles employing beamforming capabilities. At base station side vertically polarized 8 port antennas together with radio heads are employed. At UE side two fuselage mounted antennas are connected to a modem with 34 dBm transmit power [5] [6].

The network topology of air-to-ground radio networks differs from terrestrial networks. ISDs of the base stations are usually much larger and the coverage area moves from quasi 2D to 3D. Additionally the customer premise equipment (CPE) and its antennas mounted on an aerial platform will be significantly different compared to terrestrial UEs, e.g., higher antenna gain and higher transmitted radiated power (TRP)

In 2022 3GPP started its work towards specifications for ATG base station (BS) and UE [7]. Goal is to include these specifications in Rel. 18. Justifications of a separate standard for ATG are the larger inter-



site distances (ISDs), the 3D coverage area and the special CPEs at airplanes compared to a conventional terrestrial network. In addition, coexistence between ATG and terrestrial networks operating at the same frequency must be ensured. 3gpp assumes cell radii of 200-300km, focusing on 5G NR frequency bands, e.g., n1, n78 or n79. In order to define the specifications, simulations and detailed technical discussions will be carried out based on the assumptions mentioned.

The academic community has been making a lot of effort to develop solutions for NTN. The survey [8] provides an overview of the current requirements, communication technologies, system architectures, simulation platforms, and open challenges in future aerial communication networks. The survey indicates that the antenna design for aerial applications depends on the use case. For instance, directional beampatterns enable coverage in high altitudes, while broad or omni directional beams are more suitable for air-to-air links for collision avoidance. It is also pointed out that beamforming and beam tracking are relevant for reducing the number of handovers and reducing intercell interference.

The doctoral thesis [9] provides an extensive overview on ATG connectivity solutions and proposes an ATG model. Based on a link budget analysis, interference and network models, the author formulates an optimal aircraft throughput allocation problem. The problem formulation incorporates flight traces, and ground station (GS) deployments based on GoGo and EAN. The antenna model for both GS and aircraft is based on gain approximation formulas.

An evaluation of ATG networks based on LTE is provided in [10]. It discusses the design of both broadcast and traffic channels with a link budget analysis considering “pencil” beamforming supported by LTE. Moreover, a hierarchical antenna architecture is proposed for covering flights from 4 km to 12 km of altitude. It consists of a combined antenna with up tilts at 16, 33, 49, and 65 degrees. For each “sub-antenna,” the RSRP level is analyzed at a certain altitude. The proposed architecture provides better coverage than a system with a single antenna pointing its main beam to 16 degrees uptilt. A mathematical framework for ATG range extension calculation as a function of the GS antenna setup is presented in [11]. The considered antenna array model is based on an active antenna system (AAS) with full-dimension MIMO. The signal-to-noise ratio (SNR) expressions presented therein are cell-range dependent and therefore can be used to analytically calculate the minimum number of antennas necessary to achieve a certain network-level target.

The performance of NR in ATG networks is first studied in [12]. The feasibility of this radio access technology (RAT) in sub-7 GHz and mmWave ranges is evaluated. System-level evaluations indicate that large throughput in both uplink and downlink can be achieved by leveraging the large bandwidth provided by mid-band and high-band channels if an appropriately sized antenna is used. However, NR still faces some challenges that need to be addressed. These include, for example, problems with timing advance estimation and isolation between downlink and uplink slots in time division duplexing (TDD), pronounced Doppler effects on spectrum due to high mobility, and challenges related to coexistence with terrestrial and satellite systems. The paper outlines promising research directions, including aircraft UE beamforming and ATG interference management.



3 System Model

This chapter presents the system model that will guide the ATG antennas to be developed and simulated in WP2 and experimentally validated in WP5. Sections 3.1 and 3.2 discuss the network and antenna requirements that are given as inputs to the antenna design. The network requirements are related to KPIs such as downlink (DL) and uplink (UL) bitrate, and cell coverage radius, for example. The antenna requirements, on the other hand, provide mechanical and electrical design constraints demanded by practical solutions. The network, propagation, and antenna models are presented in Sections 3.3-3.5, respectively.

3.1 Network Requirements

The NGMN Alliance 5G White Paper [13] provides a description of the 5G system architecture and components examples that serve as a guideline for study and development within industry and academia. The 3D connectivity use, which includes aircraft coverage, was considered in this report. The requirements proposed by this white paper are summarized in Table 3.1. The connectivity density was calculated assuming a scenario with 20 planes in each of 3 sectors of the ground station. The traffic density considered 400 users per plane, with 20% activity factor, which gives 80 active UEs per plane, in average.

Attribute	KPI requirement
Cell-edge bitrate	DL: 15 Mbps, UL: 7.5 Mbps
End-to-end latency	10 ms
Mobility	Up to 1000 km/h
Connection density	80 UE per aircraft, 60 planes per 18000 km ²
Traffic density	DL: 1.2 Gbps/plane, UL: 600 Mbps/plane

Table 3.1 KPI requirements proposed by NGMN Alliance for the 3D connectivity use case. Table adapted from [13]

The assumptions used in the KPI requirements shown in Table 3.2 are criticized in [14]. Referring to flight statistics of Europe, the authors argue that NGMN's requirements are over ambitious. In particular, they claim that the proposed connection density is too large according to flight statistics. By contrast, the KPI requirements proposed in [14] are presented in Table 3.2. This Table considered short-haul flights in Europe with 160 passengers onboard in average and 20% activity factor.

Attribute	KPI requirement
Cell-edge bitrate	DL: 15 Mbps, UL: 7.5 Mbps
Connection density	32 UE per aircraft, 30 planes per 18000 km ²
Traffic density	DL: 480 Mbps/plane, UL: 240 Mbps/plane

Table 3.2 KPI requirements proposed in the paper [14]

As various values are proposed for cell-edge bitrate, connection density, and traffic density, the link budget analysis in Section 4.1 shall consider different scenarios with combinations of different KPI requirements and system parameters. Naturally, as the expectations on the network requirements increase, the system will demand more resources, e.g., power and bandwidth.

3.2 Antenna Requirements

The antenna requirements of ATG systems are different from those of terrestrial networks (TN). When it comes to the ground station (GS) antenna design, the main difference is that the radiated energy shall be steered towards the sky to serve flying vehicles. In addition, the GS should be carefully designed to



mitigate interference with TNs and any other system operating at neighboring frequency ranges. Unlike typical mobile handhelds terminals of TNs, the UE in ATG is airborne. This implies various mechanical and electrical requirements that complicates the aircraft antenna design. These requirements and their challenges are discussed in more details in the following sections.

3.2.1 Ground Station Antenna Requirements

As discussed in the state-of-the-Art review, the previous generation of ATG communication systems was based on 4G LTE and it was built using fixed-beam passive antennas. Back then, the antenna beam had to fulfill strict requirements to provide coverage from horizon to zenith directions. Owing to massive MIMO and active antenna systems (AAS), 5G NR networks support high-gain dynamic antenna beams to better serve the UEs compared to the previous generations. The high mobility of the aircraft and the ambitious network requirements of ATG networks demand an advanced antenna solution. Dynamic beamforming capabilities and a large effective isotropic radiated power (EIRP) are required to satisfy the requirements of modern ATG systems. Therefore, an AAS antenna shall be considered within the scope of this work package.

The design of the antenna radiator array and its beamforming weights is essential to the AAS performance. The array and its radiator elements are usually designed to satisfy requirements related to (active) return loss, cross-polarization ratio, angular and frequency bandwidth, isolation, efficiency, gain, among others. The beamforming design procedure involves the calculation of the complex-valued weights that form the far-field beam and steer it to the desired direction. These complex weights are implemented in the digital domain, i.e., baseband signal processing, and are influenced by the embedded antenna element patterns.

AAS beamforming mainly involves the design of traffic and control beams. While the former form high-gain beams to serve UEs in PDSCH and PUSCH, the latter is served to provide coverage to physical control channels. Some of the control channels and signals, e.g., SSB and RACH, need to be broadcasted around the cell area. In ATG systems, the sidelobe level should be carefully selected to avoid interference with other wireless systems, e.g., terrestrial networks and airborne systems like radio altimeter devices. To this end, AAS beamforming should conform to main lobe and sidelobe masks. The main lobe mask is designed according to the AAS dimensioning requirements, and it is explained in Section 4.2, whereas the sidelobe mask is typically chosen to satisfy co-existence and regulatory aspects. Figure 3.2.1.1 shows an example of antenna masks for the vertical and horizontal cut of a boresight beam. This example specifies regions of minimum and maximum gain requirements. The vertical cut satisfies both requirements for the considered angle width, while the horizontal cut overshoots the maximum requirement around $\pm 60^\circ$.

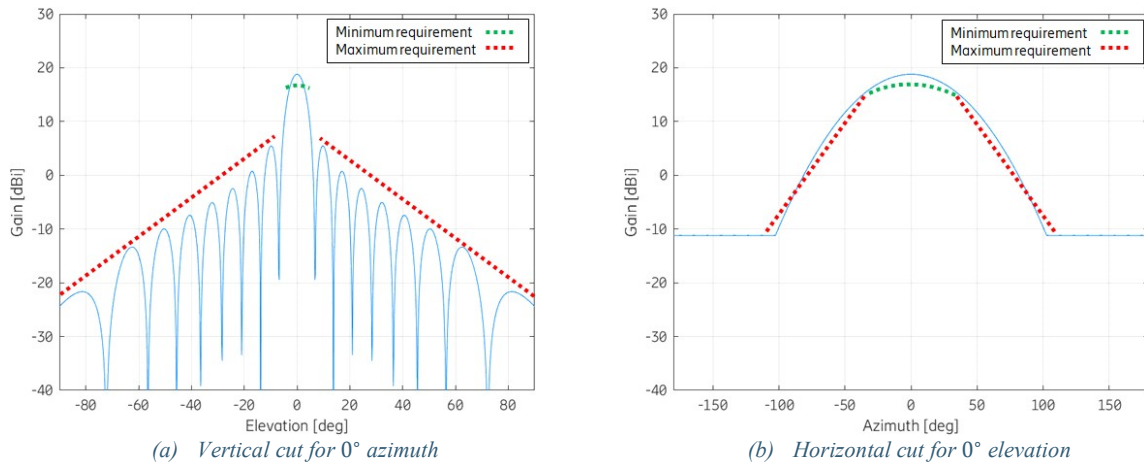


Figure 3.2.1.1 Vertical and horizontal cuts

3.2.2 Aircraft Antenna Requirements

Aircraft may connect to NR networks through a terminal cellular unit or a terminal wireless LAN unit. Depending on the unit type, its antennas are located inside the aircraft or mounted on its fuselage. In any case, the aircraft antenna shall satisfy various strict mechanical and electrical requirements in order not to interfere with other critical antenna-based systems, such as TCAS and radio altimeters. On the other hand, the airborne antenna complexity might also need to increase to achieve the network requirements. For instance, the ATG link budget might demand a large EIRP from the aircraft depending on the deployment scenario. To this end, a dynamic phased array could be implemented, implying heavier and more expensive payload.

The optimal aircraft antenna design that takes into account the position of the antenna system within the aircraft and related aerodynamic and mechanical aspects is out of the scope of this work package. The aircraft antenna design will be guided mostly by the link budget calculations and by a general option for low-complexity antenna technologies.

3.3 Network and Radio Access Technology Models

For the system-level evaluation of the antenna on an ATG system deployment, a network model based on 5G NR radio access technology (RAT) with full buffer traffic model is considered. Different network deployments can be considered for varying ISD, UE distribution, antenna configuration, among other parameters. Specific network and link parameters, such as system bandwidth, transmit power, beamforming scheme, coding and modulation scheme, CSI quality, among other parameters, shall be specified for each simulation trial. The proposed simulation framework is rather independent from the carrier frequency. However, the focus shall be on the additional spectrum that is discussed for 6G, e.g., the 6425-7125 MHz band [15]. One of the main assumptions of the network model is that only flying UEs shall be served by the ATG GS. Networks that integrate terrestrial and flying UEs are out of the scope of this work package. Nevertheless, the proposed simulation framework could still be applied to study this integrated type of network, since the different aspects between standalone and integrated ATG networks affect mostly the system requirements and system-level simulations, which are both considered in the simulation framework. The network model does not assume any specific duplexing scheme. In fact, both frequency division duplexing (FDD) and time division duplexing (TDD) have their advantages and disadvantages in the ATG use case. One of the main benefits of TDD

is the channel reciprocity-based beamforming. However, as pointed out in [12], TDD-based ATG NR systems require a guard period to isolate downlink and uplink slots, which increases the system overhead and reduces the cell throughput. By contrast, FDD-based ATG NR systems do not need guard periods between slots, and it is the duplexing choice for other NTN use cases, e.g., earth-to-satellite communications. However, it is not clear whether the feedback-based FDD CSI acquisition schemes would pose a problem in large-cell ATG deployments.

Central to the ATG antenna system are the network deployment assumptions. The GS deployment shall consider sectorized with up to 200 km of coverage radius. The ISD depends mostly on the network requirements and traffic distribution on the geographical area to be served. Site deployment parameters are also important to the AAS design. As it will be discussed in Section 4.2, the AAS in each site sector is dimensioned to fit most of the flying UEs within its main beam and the UE distribution naturally depends on the GS deployment. Since only flying UEs are served by the ATG system, the GS antennas are mechanically up tilted to better radiated the electromagnetic energy towards the sky. As discussed in [16], the antenna uptilt is employed such that the UEs are provided with a sufficiently large antenna gain that fits the capacity link budget. More specifically, considering a grid-of-beams (GoB) beamforming scheme for shared physical channels, the AAS and its beam codebook are dimensioned such that the most of the UEs are served by the half-power beamwidth (HPBW) of the codebook envelope, as illustrated in Figure 3.3.1. The AAS dimensioning and traffic codebook design will be discussed in Sections 4.2 and 4.4, respectively.

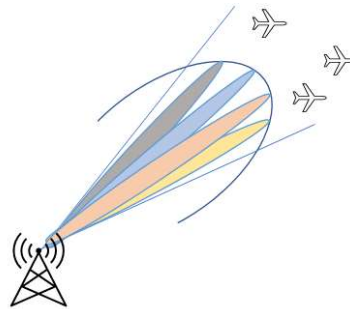


Figure 3.3.1 Ground station antenna with up-tilting serving aircraft UE.

The deployment modeling of flying UEs is more complex than terrestrial UEs. This is mainly because flying UEs are allowed to move in the 3D space at high velocities. Therefore, the classical 2D cell model depicted in Figure 3.3.2(a) needs to be extended to support flying UEs. In the presented simulation framework, UEs are assumed to be distributed according to some distribution law within a 3D region around the deployment area. For example, a uniform cylinder grid, as observed in [10] and illustrated in Figure 3.3.2(b), is considered in the AAS dimensioning discussion in Section 4.2, although any other distribution can also be used. It is important to mention that ATG systems are assumed to serve only flying UEs and, therefore, the minimum cell altitude should be chosen to minimize the likelihood of terrestrial UEs to establish a connection through an ATG link.

Other network aspects, such as interference modeling, handover management, and resource allocation, are out of the scope of this deliverable and shall be discussed in more details in the upcoming work package tasks.

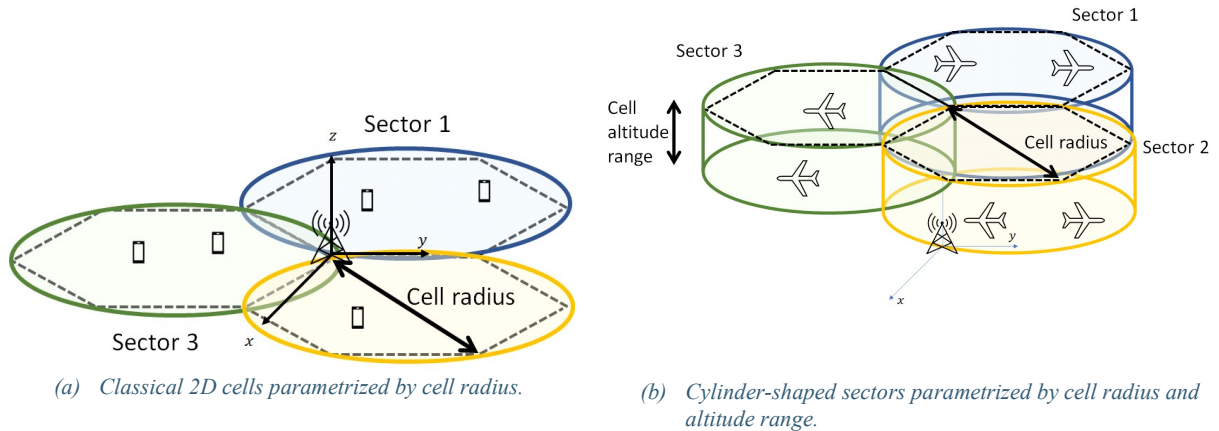


Figure 3.3.2 A ground station site with three sectors.

3.4 Propagation Model

Flying UEs in ATG are assumed to be served only in the sky, as discussed in the network model section. Considering that the ground station sites are located outdoors at some high-rise platform, it is reasonable to assume that a line of sight (LOS) between the TX and RX is available with high probability during service time.

In this case, the small-scale fading is then modeled as Rician with a weak non-LOS (NLOS) term. As discussed in [14], ATG LOS channels have a very limited number of multipaths, and, therefore, there is no significant Doppler spread. Then, the Doppler shift of the transmitted spectrum can simply be pre-compensated at the RX. The ITU-R recommendation [17] describes a series of channel models for Earth-to-space large-scale fading. There, in addition to the free-space path loss term, additional losses due to rain, cloud, and gaseous absorption attenuation are considered. Earth-to-space communication may also suffer from atmospheric scintillation and tropospheric scattering. Fortunately, most of these Earth-to-space propagation phenomena do not have a significant impact on ATG communication systems. This is mostly because aircraft seldom cross 13000 km of altitude. In the proposed simulation framework, the large-scale fading is dominated mostly by the free-space path loss with no shadowing. Margins for rain, cloud and gaseous absorptions are included in the link budget analysis of Section 4.1. More specific phenomena, such as atmospheric refraction, are not considered in the propagation model.

3.5 Antenna Array Model

The radiator array of the AAS is assumed to be partitioned into an array of sub-arrays (AoSA) [18]. Consider a uniform rectangular array (URA), with K_v rows and K_h columns of $K = K_h \cdot K_v$ dual-polarized radiators and assume that the distance between rows is denoted by d_v and between columns by d_h . The total array can be partitioned into non-overlapping sub-arrays, such that each sub-array is connected to two RF branches, one for each polarization. This way, the AAS complexity is substantially reduced for a given MIMO configuration compared to AAS that do not use partitioning, e.g., 4T4R MIMO can be implemented with both $(2 \times 1)_{SA}(2 \times 2)$ and $(3 \times 1)_{SA}(2 \times 2)$. The former setup has 8 dual-polarized elements while the latter has 12 dual-polarized elements. As discussed in Section 4.2, it is the system and deployment requirements that shall guide the array dimensioning.

It is assumed that all sub-arrays have the same number M_v of rows and M_h of columns. The antenna array is then formed by an AoSA formed by N_v rows and N_h columns of sub-arrays. Since all the sub-arrays have the same size, it follows that $K_v = M_v N_v$ and $K_h = M_h N_h$. The notation $(M_v \times M_h)_{SA}(N_v \times N_h)$ is used to represent such an array. Examples of AoSA geometries are shown in Figure 3.5.1

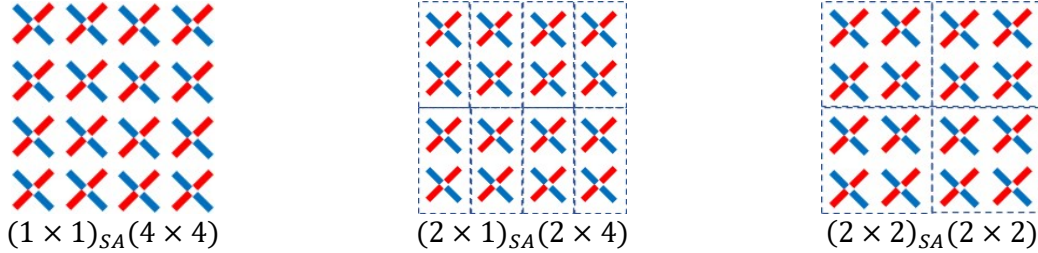


Figure 3.5.1 Array of sub-arrays examples. Each cross element represents a dual-polarized radiator.

The beamforming structure of dual-polarized AoSA is defined in both sub-array and array of sub-array levels. In the following, it is presented in a general dual-polarized notation from which single- and dual-polarized beamforming strategies can be formulated in Section 4.4. Let A and B denote the orthogonal polarization bases of the dual-polarized elements, e.g., $\pm 45^\circ$ slant, and H/V. As shown in Figure 3.5.2, each dual-polarized radiator is connected to two weight coefficients, one for each polarization. The weighting coefficients of element m in sub-array n corresponding to polarization A and B are denoted by $q_{n,m,A}$ and $q_{n,m,B}$, respectively, with $m = 1, \dots, M_h M_v$ and $n = 1, \dots, N_h N_v$. These SA weights form the two polarization ports of each sub-array and are usually implemented in the analog front-end. The sub-array weights are either fixed or slowly changing according to a remote electrical tilting (RET) functionality. For model simplicity purposes, it is assumed that, for a given polarization basis, the SA weights are the same for all SAs, e.g., $q_{n,m,A} = q_{m,A} \forall n$. The SA ports are then connected to $2N_h N_v$ RF branches providing the baseband signal branches for further processing. As illustrated in Figure 3.5.3, the weighting coefficients $p_{n,A}$ and $p_{n,B}$ are applied to the signal branches $n = 1, \dots, N_h N_v$ of polarizations A and B , respectively. These AoSA weights are dynamically adapted according to the RAT necessities and form the traffic and broadcast beams.

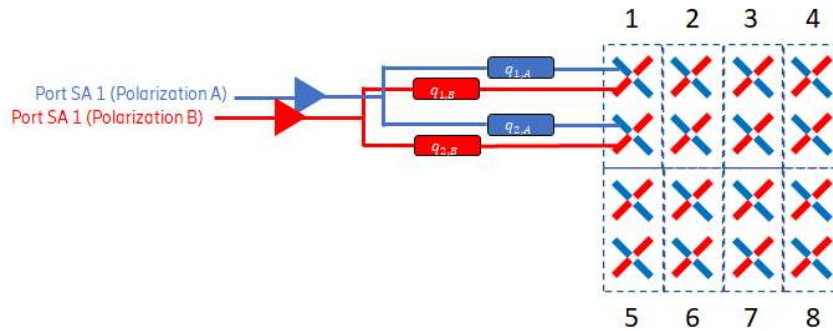


Figure 3.5.2 Sub-array weighting coefficients for an $(2 \times 1)_{SA}(2 \times 4)$ AoSA.

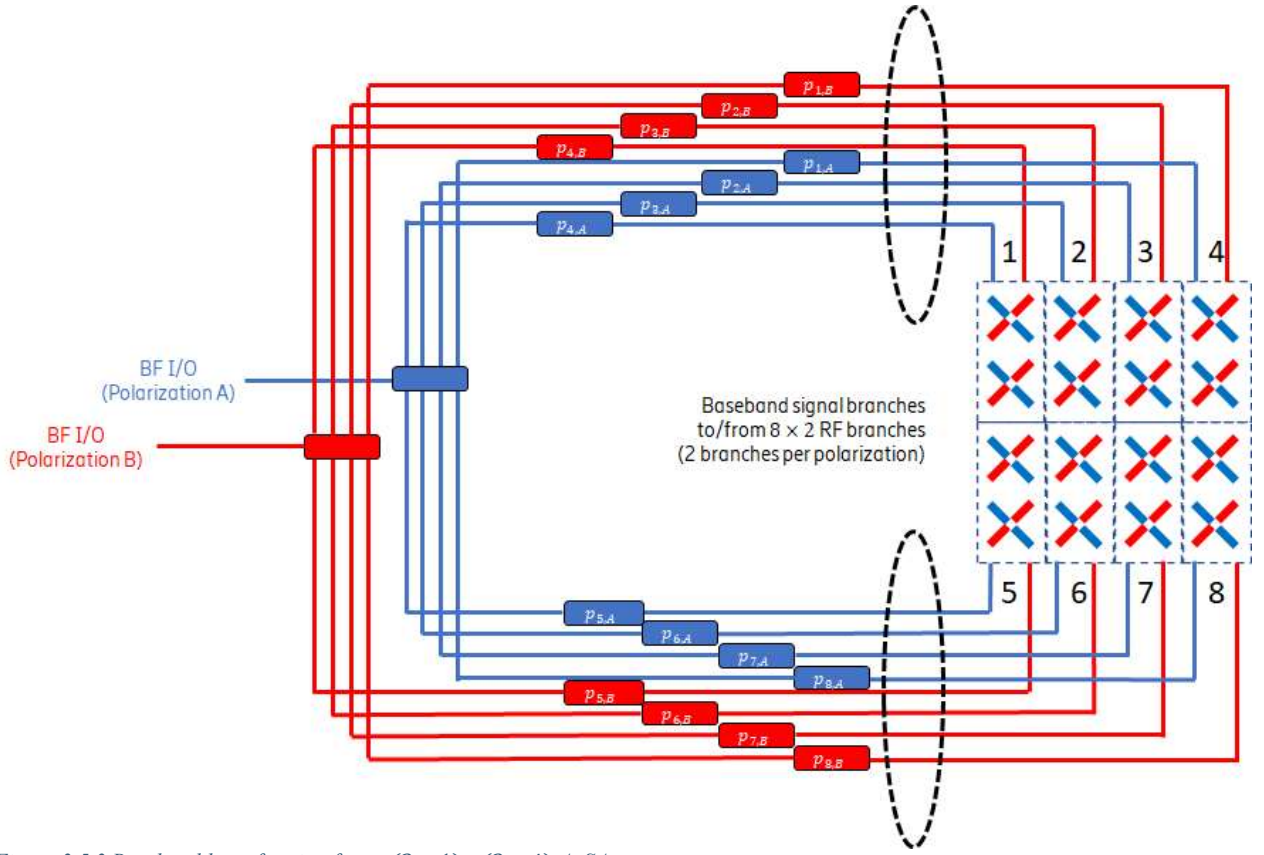


Figure 3.5.3 Baseband beamforming for an $(2 \times 1)_{SA}(2 \times 4)$ AoSA.

The gain patterns of the considered AoSA model depend on the URA dimensions, the embedded element patterns, and beamforming weights. The embedded antenna element refers to gain pattern of each radiator element considering the mutual coupling effects. It is also known as the active element pattern. Let $\mathbf{p}_A = [p_{1,A}, \dots, p_{N_h N_v, A}]^T$ and $\mathbf{q}_A = [q_{1,A}, \dots, q_{M_h M_v, A}]^T$ denote the polarization basis A AoSA and SA beamforming weights vector, respectively. The AAS beamforming K -dimensional vector for the polarization A is then defined as $\mathbf{w}_A = \mathbf{p}_A \otimes \mathbf{q}_A$, where \otimes denotes the Kronecker product. Let $\mathbf{G}_A(\theta, \phi)$ be the K -dimensional embedded antenna element matrix such that the main diagonal of the product $\mathbf{G}_A(\theta, \phi)\mathbf{G}_A^H(\theta, \phi) = \mathbf{G}_A^H(\theta, \phi)\mathbf{G}_A(\theta, \phi)$ consists of the embedded element gain pattern. Furthermore, let the K -dimensional AAS URA steering vector be denoted by $\mathbf{a}_{URA}(\theta, \phi)$. The corresponding vectors and matrices for polarization basis B are defined analogously. Then, the far-field radiated E-field for both A and B polarization bases considering the coordinate system of Figure 3.5.4 is given by the complex-valued vector

$$\mathbf{e}(\theta, \phi) = \begin{bmatrix} e_A(\theta, \phi) \\ e_B(\theta, \phi) \end{bmatrix} = \begin{bmatrix} \mathbf{w}_A^H \mathbf{G}_A(\theta, \phi) \mathbf{a}_{URA}(\theta, \phi) \\ \mathbf{w}_B^H \mathbf{G}_B(\theta, \phi) \mathbf{a}_{URA}(\theta, \phi) \end{bmatrix} = \mathbf{W}^H \mathbf{G}(\theta, \phi) \mathbf{a}(\theta, \phi) \quad (3.1)$$

where $\mathbf{W} = \text{Blkdiag}(\mathbf{w}_A, \mathbf{w}_B) \in \mathbb{C}^{2K \times 2}$ is a block-diagonal matrix formed by \mathbf{w}_A and \mathbf{w}_B , $\mathbf{G}(\theta, \phi) = \text{Blkdiag}(\mathbf{G}_A(\theta, \phi), \mathbf{G}_B(\theta, \phi)) \in \mathbb{C}^{2K \times 2K}$, and $\mathbf{a}(\theta, \phi) = [1, 1]^T \otimes \mathbf{a}_{URA}(\theta, \phi)$.

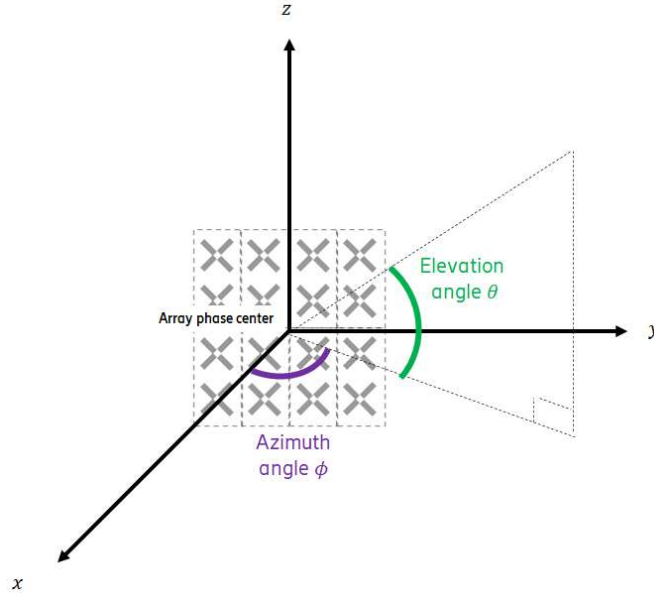


Figure 3.5.4 AAS spherical coordinates system.

The far-field AAS gain pattern is then given by

$$G(\theta, \phi) = \mathbf{e}^H(\theta, \phi)\mathbf{e}(\theta, \phi) = |\mathbf{w}_A^H \mathbf{G}_A(\theta, \phi)\mathbf{a}_{\text{URA}}(\theta, \phi)|^2 + |\mathbf{w}_B^H \mathbf{G}_B(\theta, \phi)\mathbf{a}_{\text{URA}}(\theta, \phi)|^2 \quad (3.2)$$

The steering vector $\mathbf{a}_{\text{URA}}(\theta, \phi)$ has interesting algebraic properties for an AoSA. It can be expanded as

$$\mathbf{a}_{\text{URA}}(\theta, \phi) = \mathbf{a}_{\text{AoSA}}(\theta, \phi) \otimes \mathbf{a}_{\text{SA}}(\theta, \phi) \quad (3.3)$$

where $\mathbf{a}_{\text{AoSA}}(\theta, \phi)$ the $N_h N_v$ -dimensional AoSA steering vector, and $\mathbf{a}_{\text{SA}}(\theta, \phi)$ the $M_h M_v$ -dimensional SA steering vector. The elements of these vectors are defined as

$$[\mathbf{a}_{\text{SA}}(\theta, \phi)]_{m_v+(m_h-1)M_v} = e^{jkd_h(m_h-1-\frac{M_h-1}{2})\cos\theta\sin\phi} \cdot e^{jkd_v(m_v-1-\frac{M_v-1}{2})\sin\theta} \quad (3.4)$$

$$[\mathbf{a}_{\text{AoSA}}(\theta, \phi)]_{n_v+(n_h-1)N_v} = e^{jkM_h d_h(n_h-1-\frac{N_h-1}{2})\cos\theta\sin\phi} \cdot e^{jkM_v d_v(n_v-1-\frac{N_v-1}{2})\sin\theta} \quad (3.5)$$

for $m_v = 1, \dots, M_v, m_h = 1, \dots, M_h, n_v = 1, \dots, N_v, n_h = 1, \dots, N_h$, and $k = 2\pi/\lambda$ denotes the wavenumber at center carrier frequency. Since the AoSA and the SA are bi-dimensional steering vectors, they can be further expanded in terms of their horizontal (azimuth) and vertical (elevation) directions as

$$\mathbf{a}_{\text{SA}}(\theta, \phi) = \mathbf{a}_{\text{SA,h}}(\theta, \phi) \otimes \mathbf{a}_{\text{SA,v}}(\theta) \quad (3.6)$$

$$\mathbf{a}_{\text{AoSA}}(\theta, \phi) = \mathbf{a}_{\text{AoSA,h}}(\theta, \phi) \otimes \mathbf{a}_{\text{AoSA,v}}(\theta) \quad (3.7)$$

with

$$[\mathbf{a}_{SA,h}(\theta, \phi)]_{m_h} = e^{jkd_h(m_h-1-\frac{M_h-1}{2})\cos\theta\sin\phi}, \quad [\mathbf{a}_{SA,v}(\theta)]_{m_v} = e^{jkd_v(m_v-1-\frac{M_v-1}{2})\sin\theta} \quad (3.8)$$

$$[\mathbf{a}_{AoSA,h}(\theta, \phi)]_{n_h} = e^{jkM_hd_h(n_h-1-\frac{N_h-1}{2})\cos\theta\sin\phi}, \quad [\mathbf{a}_{AoSA,v}(\theta)]_{n_v} = e^{jkd_v(n_v-1-\frac{N_v-1}{2})\sin\theta} \quad (3.9)$$

3.5.1 Equal Embedded Element Pattern Case

The AAS beampattern $G(\theta, \phi)$ in (3.2) admits a simpler expression when the embedded element pattern is the same for all elements, i.e., $\mathbf{G}_A(\theta, \phi)\mathbf{G}_A^*(\theta, \phi) = G_A(\theta, \phi)\mathbf{I}_K$ and $\mathbf{G}_B(\theta, \phi)\mathbf{G}_B^*(\theta, \phi) = G_B(\theta, \phi)\mathbf{I}_K$. In this case, (3.2) can be expressed as

$$G(\theta, \phi) = G_A(\theta, \phi)|\mathbf{w}_A^H \mathbf{a}_{URA}(\theta, \phi)|^2 + G_B(\theta, \phi)|\mathbf{w}_B^H \mathbf{a}_{URA}(\theta, \phi)|^2 \quad (3.10)$$

By plugging the definition of $\mathbf{w}_A, \mathbf{w}_B, \mathbf{a}_{URA}(\theta, \phi)$ into (3.10), it follows that

$$\begin{aligned} G(\theta, \phi) &= G_A(\theta, \phi)|(\mathbf{p}_A \otimes \mathbf{q}_A)^H [\mathbf{a}_{AoSA}(\theta, \phi) \otimes \mathbf{a}_{SA}(\theta, \phi)]|^2 + G_B(\theta, \phi)|(\mathbf{p}_B \otimes \mathbf{q}_B)^H [\mathbf{a}_{AoSA}(\theta, \phi) \otimes \mathbf{a}_{SA}(\theta, \phi)]|^2 \\ &= G_A(\theta, \phi)|[\mathbf{p}_A^H \mathbf{a}_{AoSA}(\theta, \phi)] \cdot [\mathbf{q}_A^H \mathbf{a}_{SA}(\theta, \phi)]|^2 + G_B(\theta, \phi)|[\mathbf{p}_B^H \mathbf{a}_{AoSA}(\theta, \phi)] \cdot [\mathbf{q}_B^H \mathbf{a}_{SA}(\theta, \phi)]|^2 \\ &= G_A(\theta, \phi) \cdot |AF_{AoSA,A}|^2 \cdot |AF_{SA,A}|^2 + G_B(\theta, \phi) \cdot |AF_{AoSA,B}|^2 \cdot |AF_{SA,B}|^2 \end{aligned} \quad (3.11)$$

If the AoSA and SA weights are separable, i.e., $\mathbf{p}_A = \mathbf{p}_{h,A} \otimes \mathbf{p}_{v,A}$ and $\mathbf{q}_A = \mathbf{q}_{h,A} \otimes \mathbf{q}_{v,A}$, then the array factor terms $AF_{AoSA,A}$ and $AF_{SA,A}$ can be further decomposed into their horizontal and vertical factors as [19]

$$|AF_{AoSA,A}|^2 = |AF_{AoSA,h,A}|^2 \cdot |AF_{AoSA,v,A}|^2 \quad (3.12)$$

$$|AF_{SA,A}|^2 = |AF_{SA,h,A}|^2 \cdot |AF_{SA,v,A}|^2 \quad (3.13)$$

where the horizontal and vertical array factors are defined with respect to the factors of $\mathbf{p}_A, \mathbf{q}_A, \mathbf{a}_{SA}(\theta, \phi)$, and $\mathbf{a}_{AoSA}(\theta, \phi)$ in (3.10) and (3.11). Naturally, the AF separability results corresponding to polarization basis B are obtained analogously.

3.5.2 AoSA Beampattern Examples

The examples in this section assume equal embedded element patterns for demonstration purposes.

Single-Polarized Uniform Rectangular Array Beampattern

In single-polarized beamforming, $e_B(\theta, \phi)$ in (3.1) is zero. If a separable beam weight is used, e.g., a discrete Fourier transform (DFT) beam, then (3.10) simplifies to

$$G(\theta, \phi) = G_{SA}(\theta, \phi) \cdot |AF_{AoSA,h}(\theta, \phi)|^2 \cdot |AF_{AoSA,v}(\theta, \phi)|^2 \quad (3.13)$$

$$G_{SA}(\theta, \phi) = G_A(\theta, \phi) \cdot |AF_{SA,h}(\theta, \phi)|^2 \cdot |AF_{SA,v}(\theta, \phi)|^2 \quad (3.14)$$

The horizontal and vertical array factors are obtained from (3.11)-(3.13). In Figure 3.5.5(a), the full sphere beampattern of a $(2 \times 1)_{SA}(4 \times 8)$ AoSA with $d_h = 0.5\lambda$, $d_v = 0.7\lambda$, and $\max_{\theta, \phi} G_A(\theta, \phi) =$

8 dBi without any mechanical tilting. The HPBW contour of each atom in a 32-element DFT codebook is shown in Figure 3.5.5(b).

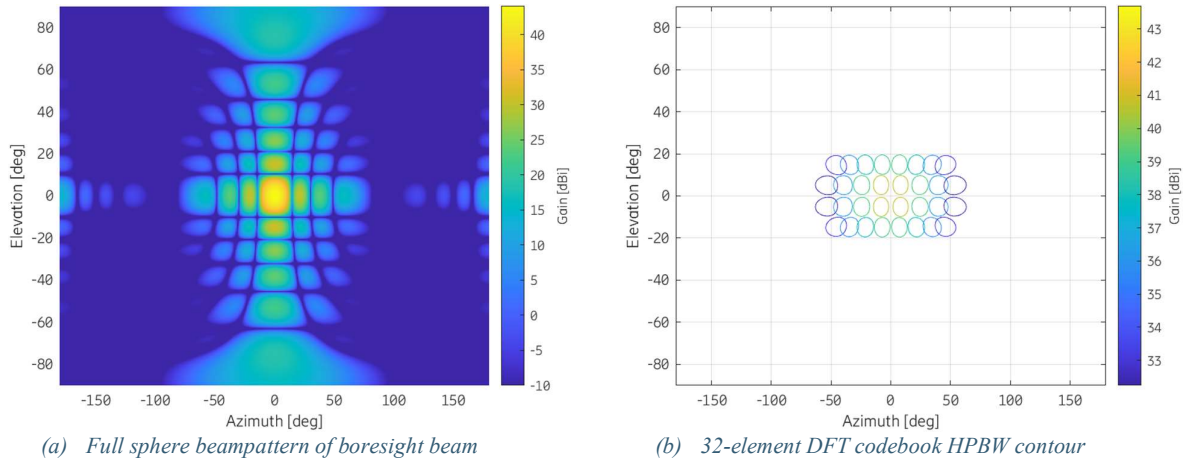


Figure 3.5.5 Example of $(2 \times 1)_{SA}(4 \times 8)$ AoSA with $d_h = 0.5\lambda$, $d_v = 0.7\lambda$.

4 Simulation Framework

The simulation framework and its components are discussed in detail throughout this section. As shown in Figure 1.1.1, the framework consists of two main steps: antenna design and system-level performance evaluation. As shown in the flowchart of Figure 4.1, the former step consists of the following procedure:

1. Link budget analysis: the antenna gains necessary to provide coverage in both uplink and control channels and achieve the network targets is calculated.
2. Antenna dimensioning: Based on the required antenna gains and network model assumptions, especially the aircraft UE distribution, the AoSA antenna dimensions are calculated.
3. Once the antenna is fully specified, then 3d antenna radiator and array modeled using CAD tools and simulated with full electromagnetic solvers. From these simulations, the embedded element patterns, which include mutual coupling effects, can be calculated.
4. The traffic and broadcast antenna beamforming weights are calculated using the embedded element patterns. They are designed to satisfy additional requirements depending on some additional system requirements.
5. Finally, the antenna beam pattern is fully specified for both traffic and broadcast channels.

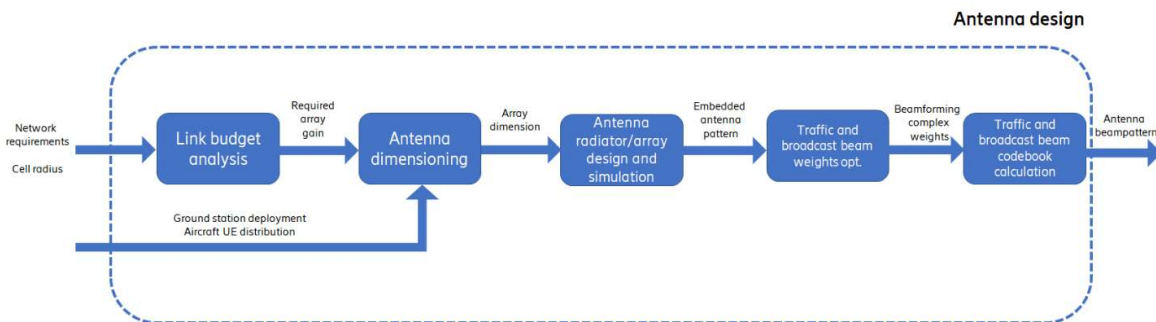


Figure 4.1 Antenna design flowchart.

The latter step is illustrated in the flowchart of Figure 4.2 and it consists of setting up a system-level simulation based on the network and RAT models of Section 3.3. This includes the configuration of propagation, traffic and deployment models with input system parameters and antenna beam patterns. By means of a network-level simulator, KPIs of the network are calculated and compared to the initial system requirements.

In case the system requirements are not fulfilled by the obtained antenna design, then the process should be repeated considering other design choices or relaxing the requirements, e.g., reducing the target cell radius and bitrate targets.

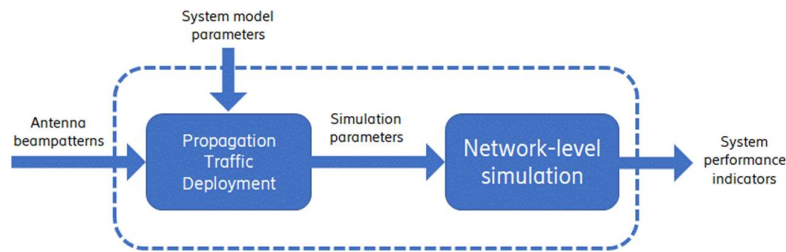


Figure 4.2 System-level performance evaluation flowchart.

4.1 Link Budget Analysis

A link budget analysis shall be performed to provide feasible cell dimensions and devise some of the antenna requirements that satisfy the system requirements. From the link budget breakdown, it is possible to determine, for example, the GS and aircraft EIRP that is necessary to provide coverage over some area above the minimum network requirements. This analysis needs to be carried out for both uplink, downlink, and control channels since they have different requirements.

Link budgets are typically calculated to guarantee that the received power is larger than the RX sensitivity. From this condition, it is possible to calculate the EIRP, and, consequently, how large should be the antenna array. Link budgets for modern mobile communication systems, however, need to guarantee that network requirements are satisfied. If cell-edge bitrate and cell throughput are considered for network requirements, then the RX signal-to-interference and noise ratio (SINR) be calculated to be larger than a certain threshold related to the requirements. In principle, this minimum SINR threshold could be analytically calculated using Information Theory, however this analysis is not trivial for modern multi-carrier 5G NR systems with adaptive modulation and coding schemes. Instead, it is usual to resort to rate maps that provide the achievable bitrate per resource block (RB) for a given SINR. These rate maps are obtained from link-level simulations performed for a specific system assumption, e.g., NR numerology, channel condition, and modulation scheme.

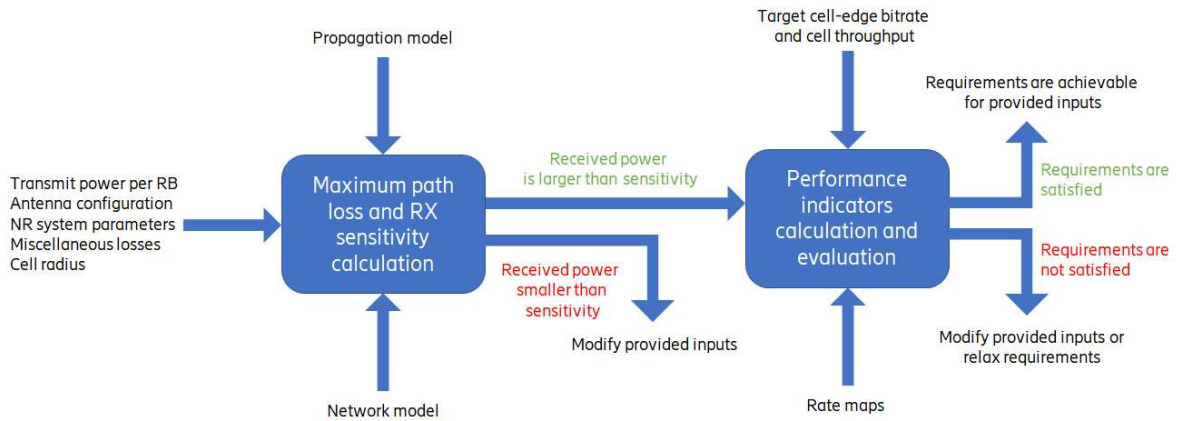


Figure 4.1.1 Link budget flowchart.

In this document, a link budget calculation methodology based on cell-edge bitrate and cell throughput requirements is discussed. In D2.2.2, this methodology shall be employed to derive the antenna requirements and assess the feasibility of different network deployments. The methodology is illustrated in Figure 4.1.1. First the received power at the RX is calculated for the given inputs and assumed network and propagation models. The inputs include transmit power per RB, antenna configuration, such as element gain and array configuration, cell radius, general NR parameters, and any miscellaneous losses that shall be included in the link budget. If the received power is larger than the RX sensibility, then the cell-edge bitrate and the cell throughput may be calculated based on the SINR, rate maps, and NR system parameters. If the requirements are satisfied, then the link budget is finalized. Else, the input parameters need to be modified or the relax requirements can be relaxed. This methodology shall be applied to both uplink and downlink traffic channels. The control channels with the same methodology but with a small modification. To check if the control channels are covered for the given input, it sufficient to check if the signal attenuation is larger than some threshold. This limit varies according to each control channel, and it is usually related to an SINR target.

4.2 AAS Dimensioning

AAS dimensioning refers to the process of calculating how many radiators the AAS will need and what is the spacing between them. The dimensioning process is carried out to fulfill two requirements:

1. The antenna array is large enough to provide the antenna gain required by the link budget.
2. The angular range of the UE distribution should be covered by the antenna array beam patterns.

The dimensioning process involves the optimization of competing parameters. For instance, consider an N -element uniform linear array (ULA) with uniform weighting and 0.5λ element spacing. The array directivity can be expressed as [20]

$$B(\psi) = E_n(\psi) \cdot AF(\psi) \quad (4.1)$$

where $\psi = \pi \cos \theta$ denotes the direction cosine, θ the steering angle, $E_n(\psi)$ the normalized element far-field directivity, and

$$AF(\psi) = \frac{\sin\left(\frac{N\psi}{2}\right)}{\sin\left(\frac{\psi}{2}\right)} \quad (4.2)$$

the array factor (AF). In Figure 4.2.1, the ULA AF is plotted for different array dimensions. As the array dimension increases, so does the array gain. However, the array HPBW decreases and, consequently, area covered by the main beam is also reduced. Also, as the array dimension increases, the total AAS might get heavier and more expensive. Therefore, the dimensioning process must strike a compromise between all these competing parameters.

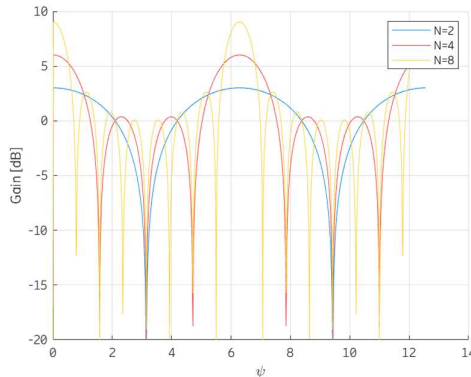


Figure 4.2.1 ULA array factor for different array sizes. Uniform weighting and 0.5λ element spacing.

The dimensioning process considers traffic beams as reference since traffic channels are usually the limiting ones. Furthermore, as detailed in Section 3.5, the AAS antenna array is modeled as AoSA. To illustrate properties of AoSAs useful for dimensioning purposes, an 8-element ULA with half-wavelength inter-element spacing is considered in the following example.

Consider a ULA with 8 dBi-gain elements and no mechanical up tilt. This array can be partitioned in four different ways, and the DFT beams supported by each partitioning are shown in Figure 4.2.3. Since the array aperture is fixed for the presented partition, the maximum array gain is the same (17 dBi), however, the HPBW of the beam codebook and the supported MIMO configuration are different. The solid black curve in these plots refer to the codebook envelope, which is defined in decibels as

$$G_e(\theta, \phi) = G_A(\theta, \phi) + 10 \log_{10} N_h + 10 \log_{10} N_v + 20 \log_{10} |AF_{SA,h}(\theta, \phi)| + 20 \log_{10} |AF_{SA,v}(\theta, \phi)| \quad (4.3)$$

The envelope HPBW is defined for some azimuth angle ϕ_0 as

$$H_e(\phi = \phi_0) = H_{\max} - H_{\min} \quad (4.4)$$

with half-power points H_{\min} and H_{\max} , such that $H_{\min} \leq H_{\max}$. Notice that the envelope HPBW comprises the main beam of a few entries in the codebook. The envelope is naturally a function of the array inter-element distances d_h, d_v and the array dimensions M_h, M_v, N_h, N_v , as well as the sub-array weights that $AF_{SA,h}(\theta, \phi)$ and $AF_{SA,v}(\theta, \phi)$.

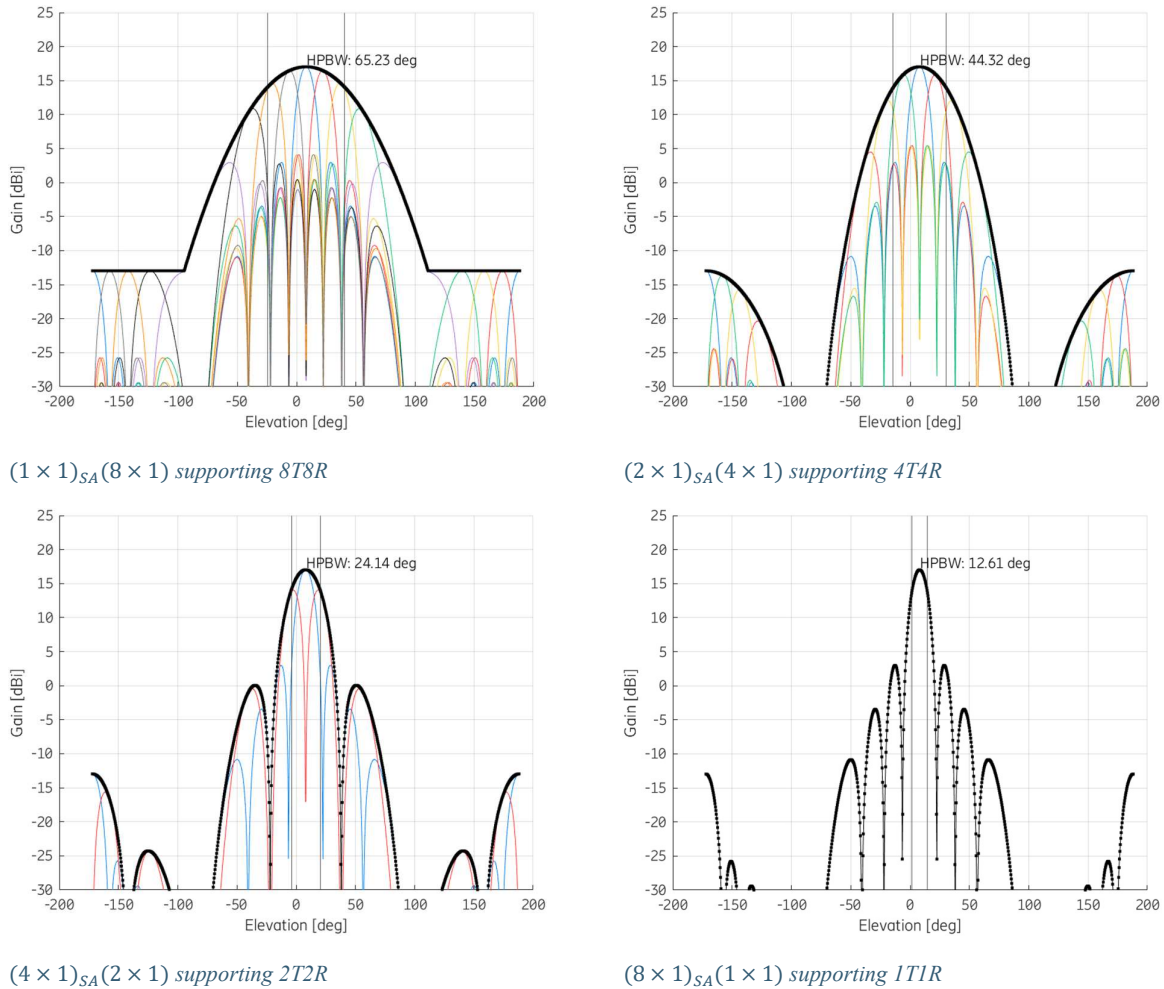


Figure 4.2.3 DFT codebook for 8-element ULA with 0.5λ element spacing.

The codebook envelope configuration depends on the deployment scenario and, specifically, on the UE spatial distribution. A deployment scenario example with different UE spatial distribution setups is presented to exemplify the AAS dimensioning process. A single 3-sector GS is considered and the UEs are assumed to be distributed within a cylinder-shape region above the GS. The simulation framework supports any UE distribution, and the following distribution is presented for example purposes. Each distribution setup is parametrized by the following values:

- ISD
- Minimum deployment altitude (z_{\min})
- Maximum deployment altitude (z_{\max})

The cylinder is uniformly sampled in the 3D space according to these parameters. The coordinate system is centered at the antenna height between the three sectors, as shown in Figure 4.2.4.

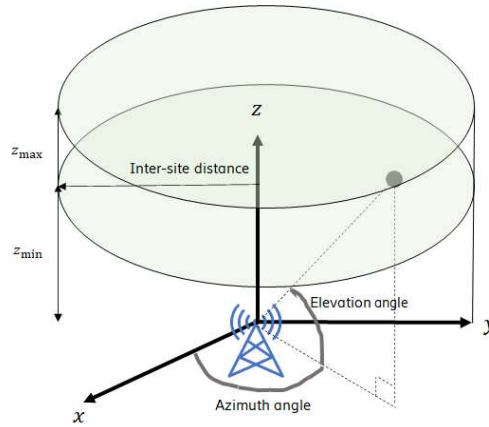


Figure 4.2.4 UE distribution setup.

Two ISD scenarios are considered:

1. 50 km ISD
2. 200 km ISD

The minimum and maximum deployment altitude are set to 3 km and 12 km, respectively, for both scenarios. The elevation and azimuth coordinates with respect to the coordinate system origin is calculated for each point in Sector 1, whose azimuth angle range goes from 0 degree to 120 degrees. The azimuth and elevation angles histograms and the point grids for both scenarios are shown in Figures 4.2.6(b) and 4.2.6(c). Due to symmetry, the statistics for Sectors 2 and 3 are the same of Sector 1.

These figures show that the azimuth angle histogram is uniformly distributed for both considered scenarios. This is natural since the distribution in the xy -plane is virtually the same. However, the elevation quite differs between both scenarios. More specifically, for the 50 km ISD scenario, the median elevation angle is 24.04 degrees, the minimum elevation is 6.79 deg, and the 95th percentile is 54.89 degrees. By contrast, for the 200 km scenario, the median elevation angle is smaller, 6.36 degrees, the minimum elevation is 1.71 deg, and the 95th percentile is 19.58 degrees. As the ISD increases, the UEs are distributed away from the site, and the GS AAS beam tends to point to boresight. On the other hand, as the ISD decreases, the UEs get closer to the site, and the GS beam tends to point towards zenith.

A procedure is proposed to cover p percent of the 3d sector region with a large gain. Considering the elevation angle distribution of some ATG deployment, let θ_{\min} denote the minimum elevation angle, and θ_p the elevation angle p^{th} percentile. The AAS mechanical up tilt is then set to

$$\theta_{\text{uptilt}} = \frac{\theta_{\min} + \theta_p}{2} \quad (4.5)$$

Furthermore, let the elevation range width be defined as $\bar{\theta} = \theta_p - \theta_{\min}$. Then, the AAS dimensioning parameters $d_h, d_v, M_h, M_v, N_h, N_v$ are designed such that the envelope codebook HPBW (4.3) approximates the elevation range width $\bar{\theta}$ for some azimuth angle ϕ_0 . The AAS dimensioning can be formulated as the following optimization problem:

$$\min_{d_h, d_v, M_h, M_v, N_h, N_v} |\bar{\theta} - H_e(\phi = \phi_0)|^2 \quad (4.6)$$

AAS dimensioning examples are provided for the deployments shown in Figures 4.2.6(d) and 4.2.7(d). It is also assumed in these examples that the link budget requires antenna gain of 23 dBi. Only one AAS column of elements with 8 dBi and DFT-based GoB beamforming are considered for presentation simplicity. For the 50 km ISD scenario, assuming 95% of coverage, the mechanical up tilt is $\theta_{\text{up tilt}} = 30.84^\circ$ and the elevation range width for $\phi_0 = 0^\circ$ is $\bar{\theta} = 48.1^\circ$. A $(2 \times 1)_{SA}(16 \times 1)$ array with 0.45λ vertical element separation yields the codebook envelope HPBW of $H_e(\phi = 0^\circ) = 49.64^\circ$ and its beams are shown in Figure 4.2.6(d). For the 200 km ISD scenario, also assuming 95% of coverage, the mechanical up tilt is $\theta_{\text{up tilt}} = 10.64^\circ$ and the elevation range width for $\phi_0 = 0^\circ$ is $\bar{\theta} = 17.18^\circ$. A $(4 \times 1)_{SA}(8 \times 1)$ array with 0.7λ vertical element separation gives the $H_e(\phi = 0^\circ) = 18.18^\circ$. The dimensioning values discussed in this section are summarized in Table 4.1.

Deployment parameters				AAS parameters				
ISD	Median elevation	Minimum elevation	95 th perc. elevation	Array configuration	Element distance	Mechanic up tilt	Codebook envelope HPBW	Full antenna gain
50 km	24.04 deg	6.79 deg	54.89 deg	$(2 \times 1)_{SA}(16 \times 1)$	0.45λ	30.84 deg	49.64 deg	23 dBi
200 km	6.36 deg	1.71 deg	19.58 deg	$(4 \times 1)_{SA}(8 \times 1)$	0.7λ	10.64 deg	18.18 deg	23 dBi

Table 4.1 Dimensioning values for the 50 km and 200 km ISD scenarios.

Even though the number of radiators in the AAS panel is 32 in both ISD scenarios, the array dimensions are different. The MIMO order is also different: the former array operates on 16T16R while the latter on 8T8R. These examples demonstrate that the AAS dimensioning strongly depends on the UE distribution and on the required antenna gain derived from the link budget analysis. The proposed AAS dimensioning procedure used in the simulation framework is outline in the flowchart of Figure 4.2.5.

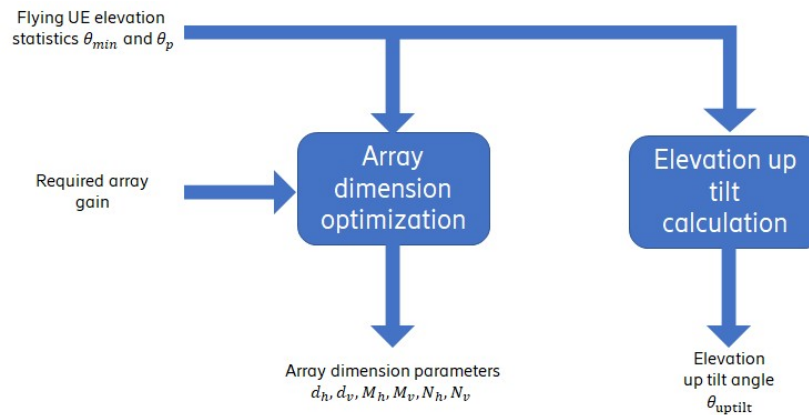
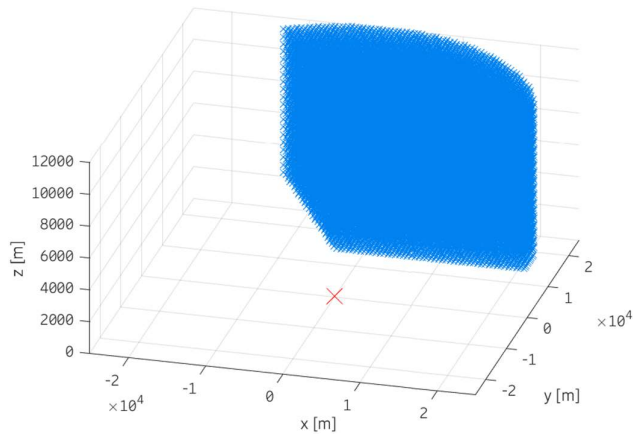
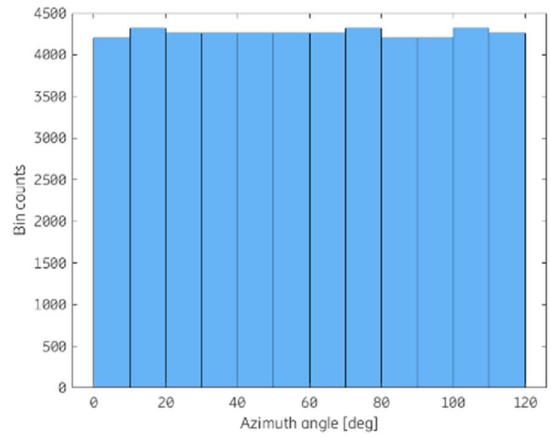


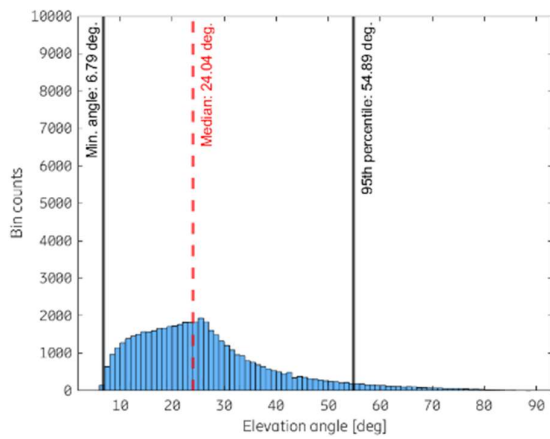
Figure 4.2.5 Antenna dimensioning procedure flowchart.



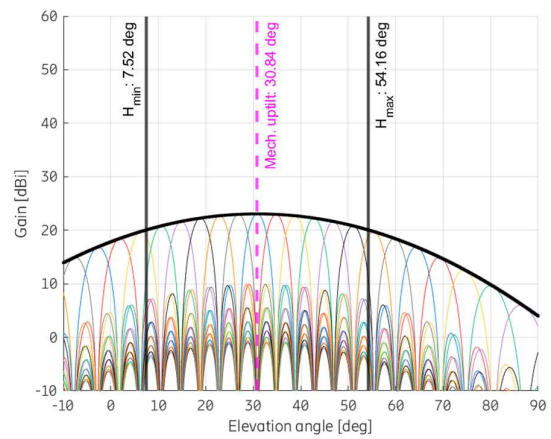
(a) UE positions (blue crosses) and site (red cross)



(b) Azimuth angle distribution

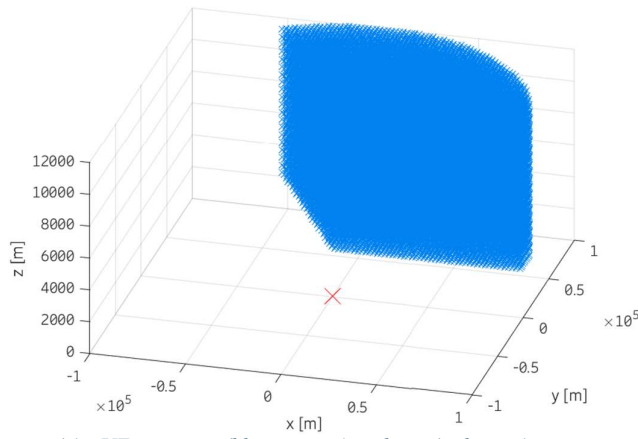


(c) Elevation angle distribution with median, minimum, and 95th percentile elevation values.

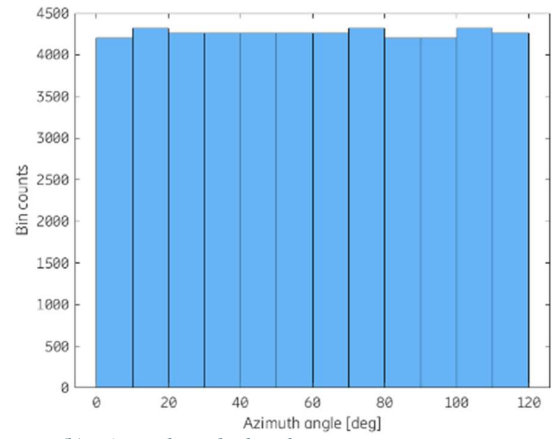


(d) Optimized AAS DFT codebook.

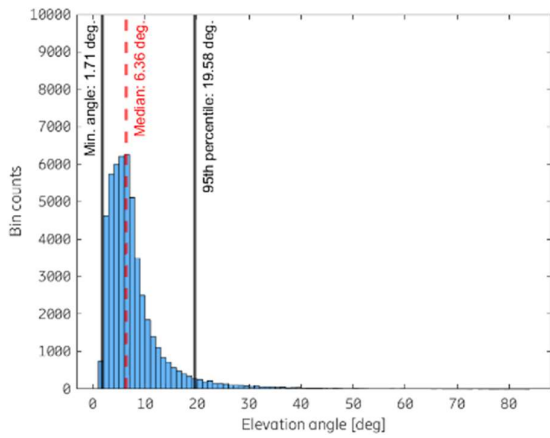
Figure 4.2.6 50 km ISD scenario.



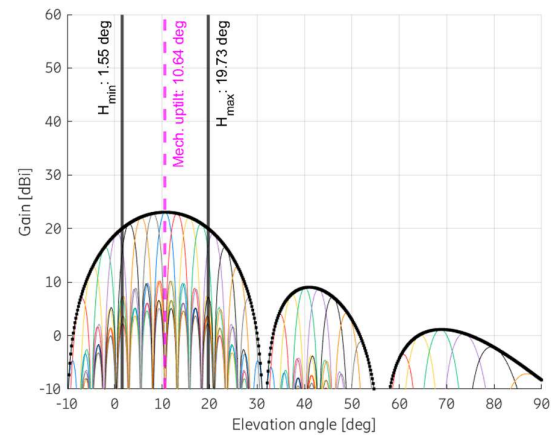
(a) UE positions (blue crosses) and site (red cross)



(b) Azimuth angle distribution



(c) Elevation angle distribution with median, minimum, and 95th percentile elevation values.



(d) Optimized AAS DFT codebook.

Figure 4.2.7 200 km ISD scenario.

4.3 Antenna Design

The 3d modeling and simulation of radiators and array methodology is presented in this section. To this end, an example design is considered. Up until this section, ULAs have been considered as examples. Now, URAs are considered in this section. The antenna can operate in the frequency range of 5.9-8.4 GHz. The vertical distance between the radiators is 0.7 times the wavelength of the center frequency and the horizontal distance between radiators is 0.5 times the wavelength of the center frequency. The distances are summarized in the following Table 4.3.1 and Figure 4.3.1.

Table 4.3.1. Separation of the radiators in the array antenna.

Ground Station Antenna	Element separation in z-direction (d_z)	Element separation in y-direction (d_y)
d in mm	29.35	21

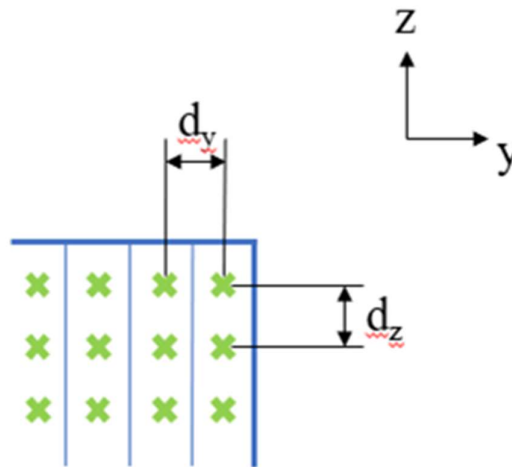


Figure 4.3.1. Distance of the radiators in the array environment.

The radiators in the antenna are grouped into a subarray of three radiators, forming a $(3 \times 1)_{SA}(1 \times 3)$ AoSA. Each of the radiators in the subarray are tapered with a different amplitude in order to create a lower sidelobe towards terrestrial users and to reduce unwanted side effects. The configuration of the subarray is shown in Figure 4.3.2. This configuration is also designed to create a more directive pattern, which focuses the radiation on the desired direction of nearly 6° .

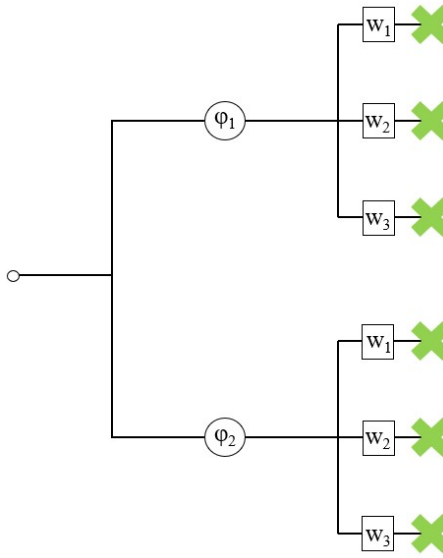


Figure 4.3.2. Subarray configuration with an integrated phase shifter.

The antenna architecture for the overall antenna system is shown in Figure 4.3.2. The subarrays are each connected with an RF port via a coupler. The RF ports are connected to the data processing unit. A small amount of power is decoupled via the coupler which is connected to a calibration network, which generally has RF dividers and switches.

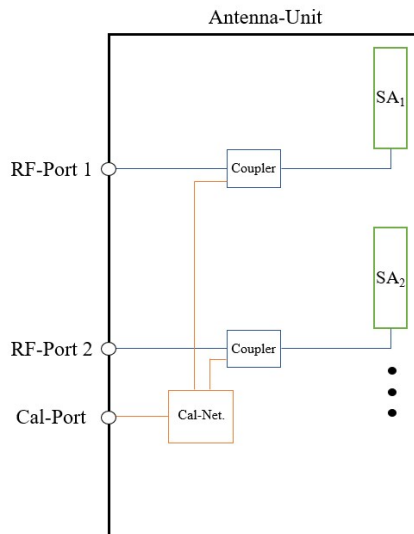


Figure 4.3.3. Antenna architecture for an ATG AAS.

To ensure reciprocity in the system, the receive and transmit paths must be calibrated to prevent mismatch in amplitude and phase. This mismatch occurs in the analog components such as the amplifiers in the transmit and receive paths. A method as used in massive MIMO antennas is shown in Figure 4.3.3. There are also other methods to calibrate the system, such as over the air measurement of the entire system.

On the flying UE side, monopole antennas are considered, as they ensure good coverage in omnidirectional direction. Since the target operating frequency is 7 GHz, it is advantageous to have a more directional beam steering on UE side so that the gain can be directed to the desired position to the base station antenna. One possible arrangement is a circular array antenna constellation, shown as in Figure 4.3.4. The phase changes would occur at the outer monopole antennas to allow beam steering. The possibility of using reactively loaded monopole antennas to implement beam steering is currently being investigated. These would have a load impedance at the outer monopole antennas, as shown in Figure 4.3.4., which would ensure the phase change.

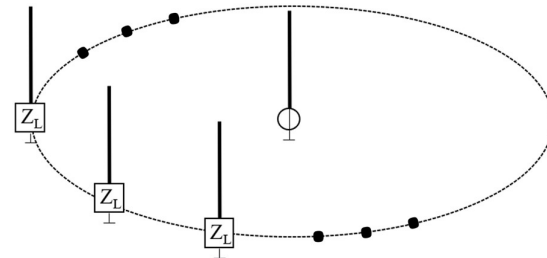


Figure 4.3.4. Architecture of a reactively loaded monopole array antenna.

4.3.1 Ground Station Antenna

During the base station antenna analysis phase, several radiator concepts were investigated and evaluated, including dipoles, slot radiators, four dipole radiators etc. All these radiator structures showed a common mode resonance in the array constellation. The common mode resonance was in the operating frequency range of the antenna, which adversely affected the antenna performance regarding the scattering parameter and far field characteristics.

The patch radiator proved to be particularly good, showing considerable improvement of shifting the resonances out of the operating band. The $(3 \times 1)_{SA}(1 \times 3)$ example is shown in the following Figure 4.3.1.1.

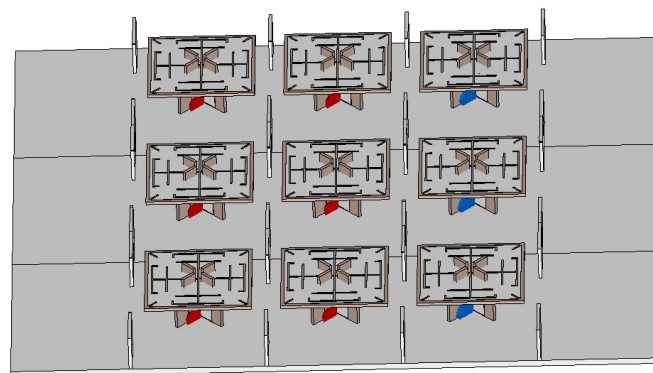


Figure 4.3.1.1. Base station array with decoupling elements.

The patch antenna is fed with a 45° crossed Roberts balun. Metal decoupling elements are provided between the patch antennas to improve the isolation between and within the columns, as well as to improve the differences in far-field characteristics between the individual columns. The next graph shows the scattering parameters of an array antenna.

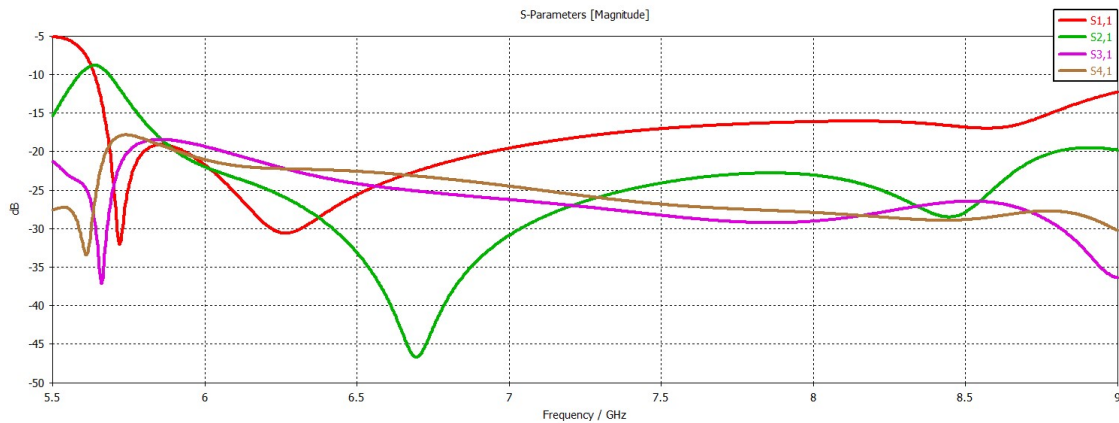


Figure 4.3.1.2. Scattering parameters of the array antenna.

The input reflection coefficient is below -15 dB for the array antenna, with isolation within the column < -18 dB. The decoupling to the neighboring column is also < -18 dB. It is important to mention that the subarray is oriented at a tilt angle of 6° . In the next graph, the far-field characteristics are shown.

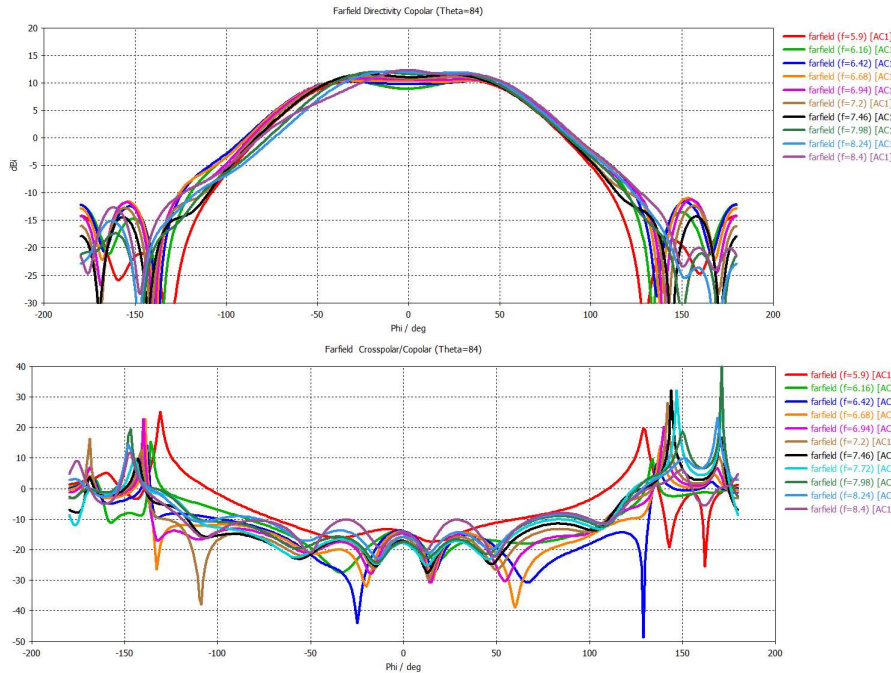


Figure 1.3.1.3. Copolar and crosspolar discrimination plots for the subarray configuration.

In the far-field characteristics the curves are very similar over frequency. Furthermore, none of the far-field characteristics are atypical, which could be due to resonance in the array antenna. The cross polar discrimination (CPD) curves show that in the main beam direction the cross polar is suppressed by < -15 dB and at $\pm 60^\circ$ by < -10 dB. Within the $\pm 60^\circ$ sector the suppression of the cross polar is < -10 dB. The next steps are to introduce a low-loss signal distribution structure, which enhances the efficiency of the antenna. The implementation and production process are currently being discussed internally.

4.3.2 Aircraft Antenna

An omnidirectional far-field pattern can be used under the aircraft, and, beyond that, an array antenna can be developed to point the main beam in the desired direction. A circular array antenna is shown in the next figure.

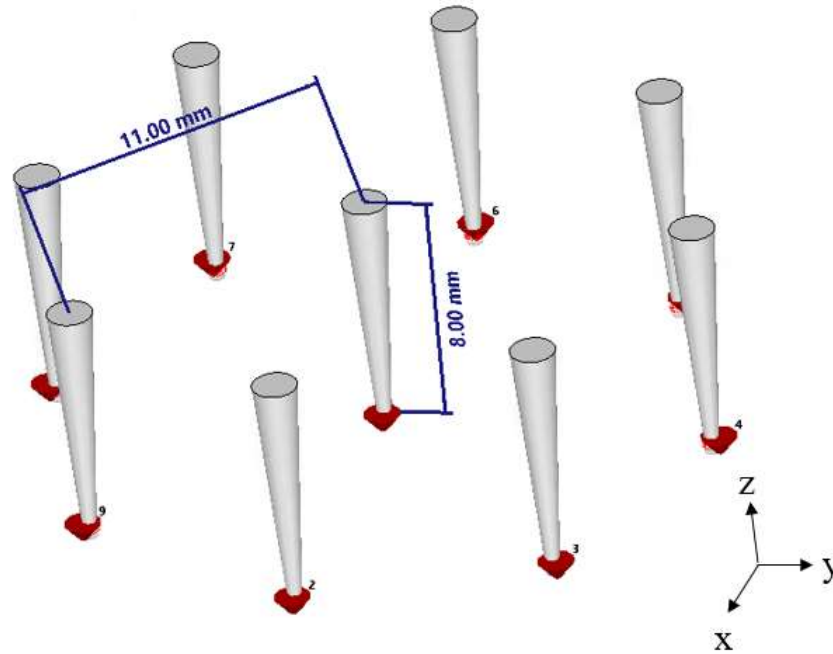


Figure 4.3.2.1. Circular monopole array.

With this arrangement, any desired scan angle can be set in the azimuth (xy plane). The next graphs show the polar as well as the cartesian diagram.

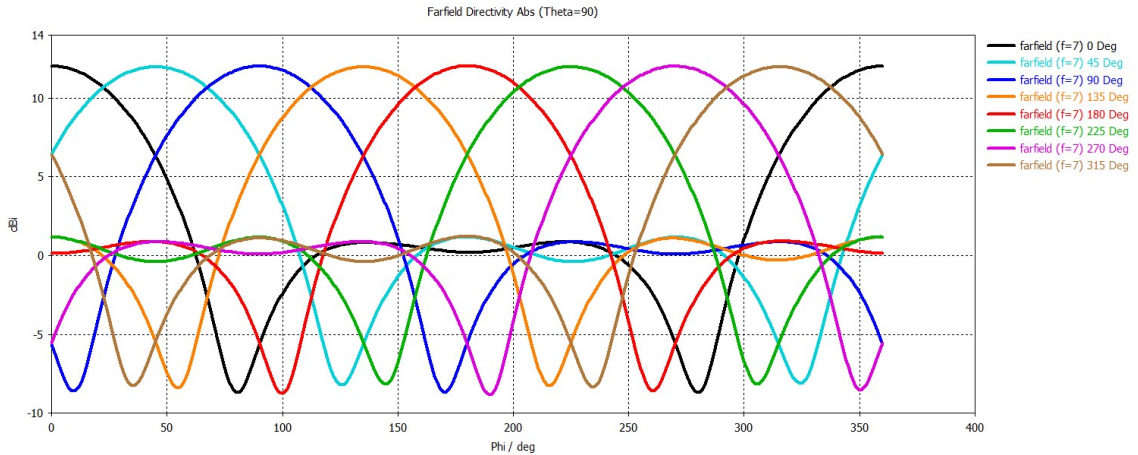


Figure 4.3.2.2. Different scan angles shown in cartesian diagram.

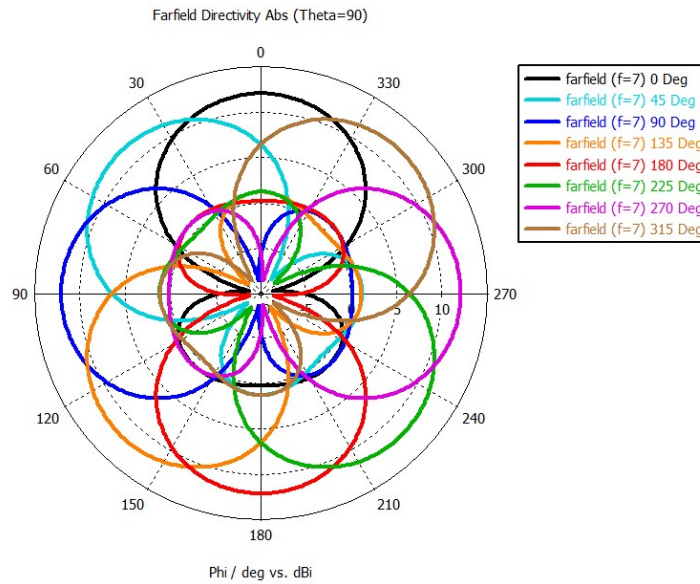


Figure 4.3.2.3. Different scan angles shown in a polar plot.

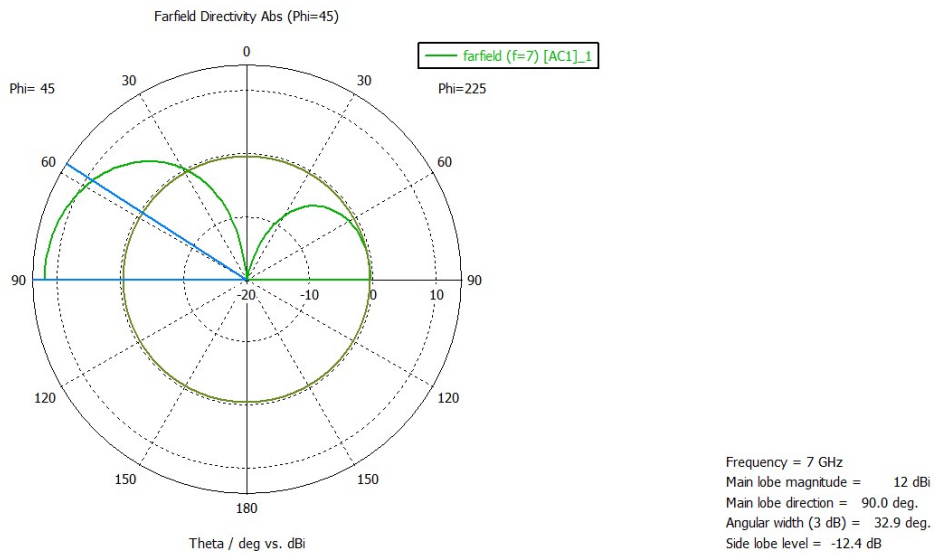


Figure 4.3.2.4. Vertical cut of the monopole array.

The entire xy plane can be steered with a higher gain. This can provide better connectivity between the ground station and the UE. The next steps are to investigate the reactively loaded group monopole antenna. In the investigation, mainly the bandwidth will be analyzed in more detail and if it is possible to use this method for the ATG use case.

4.4 Beamforming Design

The AAS radiators and finite array models are designed according to the deployment-optimized dimensions parameters and to satisfy the gain masks specified by the link budget and antenna mask. Traffic and broadcast beams have also to conform to specific antenna masks and, therefore, the corresponding complex-valued beamforming weights shall be optimized to satisfy the requirements as well. In this section, the ATG GS beamforming design problem is formulated, and possible solutions

are briefly discussed. It is assumed that the GS has perfect CSI of both UL and DL directions. The analysis and design of beamforming under imperfect CSI is out of the scope of this work. Furthermore, the digital beamforming is considered for generality purposes. Hybrid A/D beamforming can be considered in the following discussion by including the necessary beamforming constraints into the optimization problems.

The dual-polarized AoSA antenna model of Section 3.5 is considered here. AAS beamforming design shall take the following parameters as input

- Array dimensions calculated from the procedure of Section 4.2.
- Embedded array element pattern obtained from the finite EM simulations of Section 4.3 including the effects of mutual coupling.

and provide complex-valued beamforming weights that satisfy antenna gain masks requirements, and amplitude/phase constraints. A general AAS beamforming design problem for a weight variable \mathbf{w} can be expressed as

$$\begin{aligned} & \min_{\mathbf{w}} f(\mathbf{w}) \text{ subject to} \\ & g_i(\mathbf{w}) = b_i, \quad i = 1, \dots, I \\ & h_j(\mathbf{w}) \leq d_j, \quad j = 1, \dots, J \end{aligned}$$

where f is an objective function, g_i and equality constraint, and h_i and inequality constraint. The objective function and constraints depend on the target design. In the following, a few examples are provided.

4.5 Network-Level Simulator

A network-level simulator that implements the network and RAT model of Section 3.3 and the antenna model of Section 3.5 is considered in the simulation framework. The network simulations shall consider flying UE deployments, for example, as described in Section 4.2, and various GS site configurations to evaluate the different ATG AAS designs. Moreover, the antenna beam pattern of GSs and flying UEs are formed from the embedded element patterns simulated in Section 4.3 and the beamforming performed with the weighting coefficients calculated in Section 4.4. The network simulation will then provide KPIs that allow verifying whether the ATG AAS satisfies the network requirements. Specific aspects of network modeling and simulation methodology shall be further aligned with other partners in WP2 and reported in future milestones.



5 Conclusion

This document presents a detailed simulation framework for AAS design. The first NTN use case to be considered in the simulation framework is ATG communications. The simulation framework consists of two stages: AAS design and system-level performance evaluation.

In the first stage, the antenna gain requirements are derived from a link budget analysis and from antenna gain masks. The AAS dimensioning is derived from a procedure that depends on the network site deployment and flying UE distribution. Afterwards, the radiator and array are designed and simulated in a full electromagnetic solver, yielding the embedded antenna pattern elements. These serve as input to calculate the beamforming weights for traffic and broadcast beams.

In the second stage, the system parameters, the AAS embedded element beampatterns, and the beamforming weights are fed into a network-level simulator to obtain network-level KPIs. These KPIs are compared to the initial requirement to verify if the AAS design accomplishes the requirements. If not, the first step is repeated, and a new design is optimized.

The simulation framework presented in this document will be used to design new ATG AAS concepts for the next tasks in WP2.

6 References

- [1] CELTIC-Next Project 6G-Sky, "Deliverable D1.1 NTN use cases, Scenarios, and regulations," 2023.
- [2] Wikipedia, "European Aviation Network," https://de.wikipedia.org/wiki/European_Aviation_Network," 2023.
- [3] FCC, "Report on Airspan Communications Limited -ATGRU," 2022.
- [4] G. B. Aviation, "Inflight Connectivity & Entertainment," 2023.
- [5] FCC, "Report on Wireless Systems Solutions LLC -ABR0385CRM," 2020.
- [6] FCC, "Report on Wireless Systems Solutions LLC -ARRH04885CVT," 2020.
- [7] CMCC, "Revised WID on Air-to-ground network for NR," 3GPP TSG RAN Meeting #96, 2022.
- [8] A. Baltaci, E. Dinc, M. Ozger, A. Alabbasi, C. Cavdar and D. Schupke, "A survey of wireless networks for future aerial communications (FACOM)," *IEEE Communications Surveys & Tutorials*, vol. 23, p. 2833–2884, 2021.
- [9] S. Hoppe, "High-Throughput Air-to-Ground Connectivity for Aircraft," 2021.
- [10] M. Sakamoto and S. Kawato, "Four-dimensional network simulation of direct air to ground lte networks," in *2016 1st International Workshop on Link-and System Level Simulations (IWSLS)*, 2016.
- [11] H. N. Qureshi and A. Imran, "Towards designing systems with large number of antennas for range extension in ground-to-air communications," in *2018 IEEE 29th Annual International Symposium on Personal, Indoor and Mobile Radio Communications (PIMRC)*, 2018.
- [12] X. Lin, A. Furuskär, O. Liberg and S. Euler, "Sky high 5G: New radio for air-to-ground communications," *5G and Beyond: Fundamentals and Standards*, p. 503–515, 2021.
- [13] N. G. M. N. Alliance, "5G white paper," *Next generation mobile networks, white paper*, vol. 1, 2015.
- [14] E. Dinc, M. Vondra and C. Cavdar, "Total cost of ownership optimization for direct air-to-ground communication networks," *IEEE Transactions on Vehicular Technology*, vol. 70, p. 10157–10172, 2021.
- [15] N. G. M. N. Alliance, "5G white paper 2," *Next generation mobile networks, white paper*, vol. 1, 2020.
- [16] Ericsson, "Co-existence simulation parameters," 3GPP TSG-RAN WG4 Meeting #105, 2022.
- [17] ITU-R, "Recommendation ITU-R P.452-16: Prediction procedure for the evaluation of interference between stations on the surface of the Earth at frequencies above about 0.1 GHz," ITU-R, 2015.
- [18] H. Asplund, D. Astely, P. von Butovitsch, T. Chapman, M. Frenne, F. Ghasemzadeh, M. Hagström, B. Hogan, G. Jongren, J. Karlsson and others, *Advanced antenna systems for 5G network deployments: bridging the gap between theory and practice*, Academic Press, 2020.
- [19] L. N. Ribeiro, A. L. F. de Almeida, J. A. Nossek and J. C. M. Mota, "Low-Complexity separable beamformers for massive antenna array systems," *IET Signal Processing*, vol. 13, p. 434–442, 2019.
- [20] C. A. Balanis, *Antenna theory: analysis and design*, John Wiley & sons, 2015.